Thermodynamics of Proton and Electron Transfer in Tetranuclear Clusters with Mn–OH_2/OH Motifs Relevant to H_2O Activation by the Oxygen Evolving Complex in Photosystem II

Christopher J. Reed, and Theodor Agapie*

Division of Chemistry and Chemical Engineering, California Institute of Technology

Pasadena, California 91125, United States, Email: agapie@caltech.edu

Supporting Information

Table of Contents

Experimental Procedures

General Considerations

All reactions were performed at room temperature in an N_2-filled M. Braun glovebox or using standard Schlenk techniques unless otherwise specified; reactions of compounds in THF/H_2O mixtures were performed in an N_2-filled VAC wetbox. Glassware was oven dried at 140 ºC for at least 2 h prior to use, and allowed to cool under vacuum. **[LFe$_3$(OAc)(OTf)][OTf]**[1], $Mn(OTf)_2$ • 2 MeCN[2], benzyl potassium[3], iodosobenzene[4], silver tetrakis[3,5-bis(trifluoromethyl)phenyl]borate bis-acetonitrile ($Ag[BAr^F_4]$ • 2 MeCN)[5], 2,4,6-tri-tert-butylphenoxy radical (2,4,6-TBPR)[6], and tetrapropylammnoium tetrakis[3,5-bis(trifluoromethyl)phenyl]borate ($[^nPr_4N][BAr^F_4]$)[7] were prepared according to literature procedures. All organic solvents were dried by sparging with nitrogen for at least 15 minutes, then passing through a column of activated A2 alumina under positive N_2 pressure. ^{1}H and ^{19}F NMR spectra were recorded on a Varian 300 MHz spectrometer. ^{1}H NMR spectra in THF/C_6D_6 were recorded on a Varian 500 MHz spectrometer using solvent suppression protocols. CD_3CN, CD_2Cl_2, and C_6D_6 were purchased from Cambridge Isotope Laboratories, dried over calcium hydride, degassed by three freeze-pump-thaw cycles, and vacuum transferred prior to use.

Physical Methods

Mössbauer measurements. Zero field ^{57}Fe Mossbauer spectra were recorded at 80 K in constant acceleration mode on a spectrometer from See Co (Edina, MN) equipped with an SVT-400 cryostat (Janis, Wilmington, WA). The isomer shifts are relative to the centroid of an α-Fe foil signal at room temperature. Samples were prepared by mixing polycrystalline material (20 mg) with boron

nitride in a cup fitted with screw cap or freezing a concentrated solution in MeCN or THF. The data were fit to Lorentzian lineshapes using WMOSS (www.wmoss.org).

Electrochemical measurements. CVs and SWVs were recorded with a Pine Instrument Company AFCBP1 biopotentiostat with the AfterMath software package. All measurements were performed in a three electrode cell, which consisted of glassy carbon (working; ø = 3.0 mm), silver wire (counter) and bare platinum wire (reference), in a N_2 filled M. Braun glovebox at RT. Either the ferrocene/ferrocinium (Fc/Fc^+) or decamethylferrocene/decamethylferrocinium (Fc^*/Fc^{*+}; -0.524 V vs Fc/Fc^+ in THF/250 mM H_2O, under our experimental conditions) redox waves were used as an internal standard for all measurements.

X-ray crystallography. X-ray diffraction data was collected at 100 K on a Bruker PHOTON100 CMOS based diffractometer (microfocus sealed X-ray tube, Mo Kα (λ) = 0.71073 Å or Cu Kα (λ) = 1.54178 Å). All manipulations, including data collection, integration, and scaling, were carried out using the Bruker APEXII software. Absorption corrections were applied using SADABS. Structures were solved by direct methods using XS (incorporated into SHELXTL) and refined by using ShelXL least squares on Olex2-1.2.7 to convergence. All non-hydrogen atoms were refined using anisotropic displacement parameters. Hydrogen atoms were placed in idealized positions and were refined using a riding model. Due to the size of the compounds most crystals included solvent-accessible voids that contained disordered solvent. In most cases the solvent could be modeled satisfactorily.

Experimental Procedures

Potassium pyrazolate (KPz). 1.09 g (16.0 mmol) pyrazole was dissolved in 2 mL THF. To this stirring solution, a 10 mL THF solution of benzyl potassium, 2.03 g (15.6 mmol), was added dropwise; an off-white precipitate formed. After stirring for 20 minutes, the reaction was concentrated to 10 mL; the solids were collected on a glass frit and washed with 2 mL THF. The white solid was dried completely under vacuum to obtain 1.37 g (83% yield) potassium pyrazolate. Anal. calcd. (%) for $C_3H_3KN_2$: C. 33.94; H, 2.85; N, 26.39. Found: C, 34.12; H, 2.89; N, 25.38.

$[LFe_3O(Pz)_3Mn][OTf]_2$ (2-[OTf]). A suspension of 387 mg (0.28 mmol) **$[LFe_3(OAc)(OTf)][OTf]$** in 7 mL THF was stirred with 98.4 mg (0.29 mmol) $Ca(OTf)_2$ for an hour before being frozen with LN_2. To this mixture, 93.2 mg (0.88 mmol) KPz was added in thawing THF (4 mL) and stirred for 20 minutes at room temperature to obtain a dark red-orange solution. Iodosylbenzene, 63.6 mg (0.29 mmol), was added with 1 mL THF and the reaction was stirred for 90 minutes. 160 mg (0.37 mmol) $Mn(OTf)_2 \bullet 2$ MeCN solution in 2 mL THF was then added to the reaction. After 18 hours, the reaction was concentrated to 10 mL and filtered over a bed of celite; the precipitate was dried under vacuum, extracted with 8 mL DCM, and recrystallized via vapor diffusion of Et_2O into the filtrate. Dark green crystals of **2-[OTf]** were collected on a glass frit and dried (147 mg, 33% yield). Another 69 mg of **2-[OTf]** can be obtained by drying the crude reaction filtrate, extracting with 6 mL DCM and recrystallizing via Et_2O vapor diffusion (46% overall yield). X-ray diffraction quality crystals were obtained via oxidation of $[LFe_3O(Pz)_3Mn][OTf]$ (**1-[OTf]**) with 1 equivalent of $AgBPh_4$; Et_2O vapor diffusion into a DCM/THF solution of the resulting $[LFe_3O(Pz)_3Mn][OTf][BPh_4]$ produced crystals of suitable quality. ^{1}H NMR (300 MHz, CD_3CN): δ 120.8 (br), 80.8 (br), 71.0, 70.1, 52.9, 52.3, 42.2, 28.0 (br), 15.5, 13.0, 10.4, 8.1 (br), 4.38, 3.01, -2.51 (br). UV-Vis (MeCN) [ε (M^{-1} cm^{-1})] 241 nm

(6.53× 10^4), 368 nm (6.49 × 10^3). Anal. calcd. (%) for $C_{68}H_{48}F_6Fe_3MnN_{12}O_{10}S_2$: C. 51.25; H, 3.04; N, 10.55. Found: C, 50.81; H, 3.12; N, 10.18.

[$LFe_3O(Pz)_3Mn$][OTf] (1-[OTf]). A suspension of [$LFe_3O(Pz)_3Mn$][$OTf]_2$ (**2-[OTf]**; 91.5 mg, 0.057 mmol) in 2 mL THF was stirred as a THF solution of 10.9 mg $CoCp_2$ (0.058 mmol) was added. After 1 hour, the reaction was dried under vacuum. 4 mL DME was added to the purple solid and stirred for 12 hours. The resulting purple precipitate was collected on a bed of celite, washed with 2 mL DME, dried, and eluted with 2:1 THF/MeCN; crystals of [$LFe_3O(Pz)_3Mn$][OTf] (**1-[OTf]**) were obtained by vapor diffusion of Et_2O into this solution (46.3 mg, 56% yield). ^{1}H NMR (300 MHz, CD_3CN): δ 96.4 (br), 57.8, 55.5, 37.8 (br), 36.4, 34.3, 34.0, 25.2, 13.4, 13.0, 12.0, 11.4, 3.4, 2.6, -6.4 (br). UV-Vis (MeCN) [ε (M^{-1} cm^{-1})] 250 nm (6.08 × 10^4), 517 nm (3.72 × 10^3). Anal. calcd. (%) for $C_{67}H_{48}F_3Fe_3MnN_{12}O_7S$: C, 55.70; H, 3.35; N, 11.63. Found: C, 55.36; H, 3.58; N, 11.20.

[$LFe_3O(Pz)_3Mn$][$OTf]_3$ (3-[OTf]). 9.2 mg (0.036 mmol) of AgOTf in THF was added to a stirring suspension of 56.8 mg (0.036 mmol) [$LFe_3O(Pz)_3Mn$][$OTf]_2$ (**2-[OTf]**) in THF. The resulting brown suspension was pumped down after 30 minutes. The reaction was filtered over a celite pad using DCM and the solvent was removed under reduced pressure. Crystals of [$LFe_3O(Pz)_3Mn$][$OTf]_3$ were obtained via vapor diffusion of Et_2O into a concentrated DCM/MeCN solution of the crude product, 57.4 mg (92% yield). ^{1}H NMR (300 MHz, CD_2Cl_2): δ 162.2 (br), 118.9 (br), 81.2, 76.9, 74.4, 73.1, 45.7, 18.8 (br), 16.3, 9.5, 3.34, 1., -6.5 (br). UV-Vis (MeCN) [ε (M^{-1} cm^{-1})] 241 nm (7.84 × 10^4), 411 nm (9.22 × 10^3). Anal. calcd. (%) for $C_{69}H_{48}F_9Fe_3MnN_{12}O_{13}S_3$: C, 47.55; H, 2.78; N, 9.64. Found: C, 47.57; H, 3.07; N, 9.21.

[$LFe_3O(Pz)_3Mn$] (4). 4.1 mg (0.18 mmol) sodium metal was mixed ~6 g elemental mercury with a pre-reduced stirbar. After 12 hours, a 5 mL THF suspension of [$LFe_3O(Pz)_3Mn$][$OTf]_2$ (**2-[OTf]**;

114 mg, 0.07 mmol) was added to the Na/Hg amalgam. Over 4 hours, a blue precipitate formed; this resulting suspension was decanted from the amalgam and filtered over a fine porosity glass frit. The solids were washed with 5 mL THF and dried under vacuum. The resulting blue material, [$LFe_3O(Pz)_3Mn$] (78.1 mg; 84% yield), is insoluble or unstable in most typical organic solvents. Anal. calcd. (%) for $C_{66}H_{48}Fe_3MnN_{12}O_4$: C. 61.18; H, 3.73; N, 12.94. Found: C, 60.44; H, 3.82; N, 12.87

[$LFe_3O(Pz)_3Mn$][BAr^F_4] (1-[BAr^F_4]). 14.0 mg (0.013 mmol) Ag[BAr^F_4] • 2 MeCN in 2 mL Et_2O was added to a stirring suspension of [$LFe_3O(Pz)_3Mn$] (**4**; 17.2 mg, 0.013 mmol); the blue suspension changed to a purple solution. After 15 minutes, the solvent was removed under reduced pressure. 3 mL Et_2O was added to the purple residue and filtered over a pad of celite. The filtrate was dried to afford [$LFe_3O(Pz)_3Mn$][BAr^F_4] as a purple solid, 26.5 mg (92% yield). ^{1}H NMR (300 MHz, CD_3CN) is identical to [$LFe_3O(Pz)_3Mn$][OTf] (**1-[OTf]**). Anal. calcd. (%) for $C_{98}H_{60}BF_{24}Fe_3MnN_{12}O_4$: C. 54.52; H, 2.80; N, 7.79. Found: C, 54.06; H, 2.84; N, 7.33.

[$LFe_3O(Pz)_3Mn$][BAr^F_4]$_2$ (2-[BAr^F_4]). 45.0 mg (0.043 mmol) Ag[BAr^F_4] • 2 MeCN in 2 mL Et_2O was added to a stirring suspension of [$LFe_3O(Pz)_3Mn$] (**4**; 27.6 mg, 0.021 mmol); the blue suspension changed to a brown-green solution. After 15 minutes, the solvent was removed under reduced pressure. 3 mL Et_2O was added to the brown residue and filtered over a pad of celite. 6 mL benzene was added to the filtrate to produce an oily precipitate; after 30 minutes, the supernatant was removed and the remaining brown-green residue was dried under reduced pressure. 36.6 mg (57% yield) of the brown-green solid, **2-[BAr^F_4]**, was obtained; the ^{1}H NMR (300 MHz, CD_3CN) is identical to [$LFe_3O(Pz)_3Mn$][OTf]$_2$ (**2-[OTf]**). UV-Vis (THF/250 mM H_2O) [ε (M^{-1} cm^{-1})] 368 nm (5.11×10^3). Anal. calcd. (%) for $C_{130}H_{72}B_2F_{48}Fe_3MnN_{12}O_4$: C. 51.67; H, 2.40; N, 5.56. Found: C, 51.38; H, 2.56; N, 5.46.

[$LFe_3O(Pz)_3Mn][BAr^F{}_4]_3$ (3-[$BAr^F{}_4$]). 6.4 mg (0.006 mmol) [$^{Ac}Fc][BAr^F{}_4$] in 0.5 mL THF was added to [$LFe_3O(Pz)_3Mn][BAr^F{}_4]_2$ (**2-[$BAr^F{}_4$]**; 18.6 mg, 0.006 mmol). After 10 minutes, 5 mL benzene was added to the solution to produce an oily brown precipitate; after 30 minutes, the yellow supernatant was removed and the remaining brown residue was dried under reduced pressure. 18.4 mg of a brown solid was obtained (77% yield). ^{1}H NMR (500 MHz, THF/C_6D_6 [250mM H_2O]): δ 83.8, 78.2, 75.9, 50.2, 24.9 (br), 16.6, 9.8 (br), 0.1. UV-Vis (THF/250 mM H_2O) [ε (M^{-1} cm^{-1})] 405 nm (7.64×10^3). Anal. calcd. (%) for $C_{162}H_{84}B_3F_{72}Fe_3MnN_{12}O_4$: C. 50.08; H, 2.18; N, 4.33. Found: C, 50.34; H, 2.38; N, 4.29.

[$LFe_3O(Pz)_3Mn(OH)][BAr^F{}_4$] (6-[$BAr^F{}_4$]). Addition of 100 µL of a 50 mM solution of DBU in THF/250 mM H_2O to 2 mL 2 mM solution of [$LFe_3O(Pz)_3Mn][BAr^F{}_4]_2$ (**2-[$BAr^F{}_4$]**) in THF/250 mM H_2O leads to a color change of the solution from green to red. Crystals for X-ray diffraction (**6-[OTf]**) were obtained by conducting the analogous reaction with [$LFe_3O(Pz)_3Mn][OTf]_2$ (**2-[OTf]**) and DBU in 95:5 MeCN/H_2O and crystalizing via vapor diffusion of Et_2O into this solution; considerable decomposition occurs on the timescale of crystallization, making crystallization unsuitable for preparing analytically pure solid samples of [$LFe_3O(Pz)_3Mn(OH)][OTf]$. Solutions of [$LFe_3O(Pz)_3Mn(OH)][BAr^F{}_4$] were prepared for electrochemistry experiments by stirring 4 mL of 2.5 mM [$LFe_3O(Pz)_3Mn][[BArF4]]_2$ (**2-[$BAr^F{}_4$]**) and 0.1 M [$^nPr_4N][BAr^F{}_4$] solution in THF/250 mM H_2O with ~2 mg of solid KOH pellet for 1 hour; the resulting red solution was decanted off the remaining KOH before electrochemical measurements were conducted. ^{1}H NMR (500 MHz, THF/C_6D_6 [250mM H_2O]): δ 153.1 (br), 102.7 (br), 85.9, 80.0, 64.8, 60.8, 58.1, 57.3, 23.0, 15.7. 12.5, 10.9 (br). UV-Vis (THF/250 mM H_2O) [ε (M^{-1} cm^{-1})] 467 nm (3.29×10^3).

[$LFe_3O(Pz)_3Mn(OH)]$ (5). Addition of 11 mg (0.03 mmol) decamethylcobaltocene in THF/250 mM H_2O to 4 mL 7 mM solution of [$LFe_3O(Pz)_3Mn(OH)][BAr^F{}_4$] (**6-[$BAr^F{}_4$]**; 0.03 mmol) in

THF/250 mM H_2O leads to a color change of the solution from red to blue. The reaction was pumped down after 30 minutes. ^{1}H NMR (500 MHz, THF/C_6D_6 [250mM H_2O]): δ 126.0 (br), 76.1 (br), 59.6, 49.0, 46.9, 42.7, 37.0, 23.9 (br), 17.2, 15.6, 12.8, -14.9.

[LFe$_3$O(Pz)$_3$Mn(OH)][BAr$^F{}_4$]$_2$ (7-[BAr$^F{}_4$]). *Method A.* Addition of 160 μL of a 50 mM solution of Et_3N in THF/250 mM H_2O to 2 mL 2 mM solution of [LFe$_3$O(Pz)$_3$Mn][BAr$^F{}_4$]$_3$ (**3-[BAr$^F{}_4$]**) in THF/250 mM H_2O leads to a color change of the solution from brown to brown-green. ^{1}H NMR spectroscopy confirms complete conversion to [LFe$_3$O(Pz)$_3$Mn(OH)][BAr$^F{}_4$]$_2$.

Method B. Addition of 200 μL of 6 mM solution of Ag[BArF4] • 2 MeCN in THF/250 mM H_2O to 400 μL of a 3mM solution of [LFe$_3$O(Pz)$_3$Mn(OH)][BAr$^F{}_4$] (**6-[BAr$^F{}_4$]**) in THF/250 mM H_2O leads to formation of a grey precipitate. Filtration of this solution yields a brown-green solution with an identical ^{1}H NMR obtained from Method A. ^{1}H NMR (500 MHz, THF/C_6D_6 [250 mM H_2O]: δ 110.2 (br), 89.1, 85.1, 70.0, 67.2, 62.0, 19.1 (br), 15.7, 13.1, 9.8 (br), 8.6 (br), 6.2 (br), 1.1, 0.7, 0. UV-Vis (THF/250 mM H_2O) [ε (M^{-1} cm^{-1})] 389 nm (5.29×10^3).

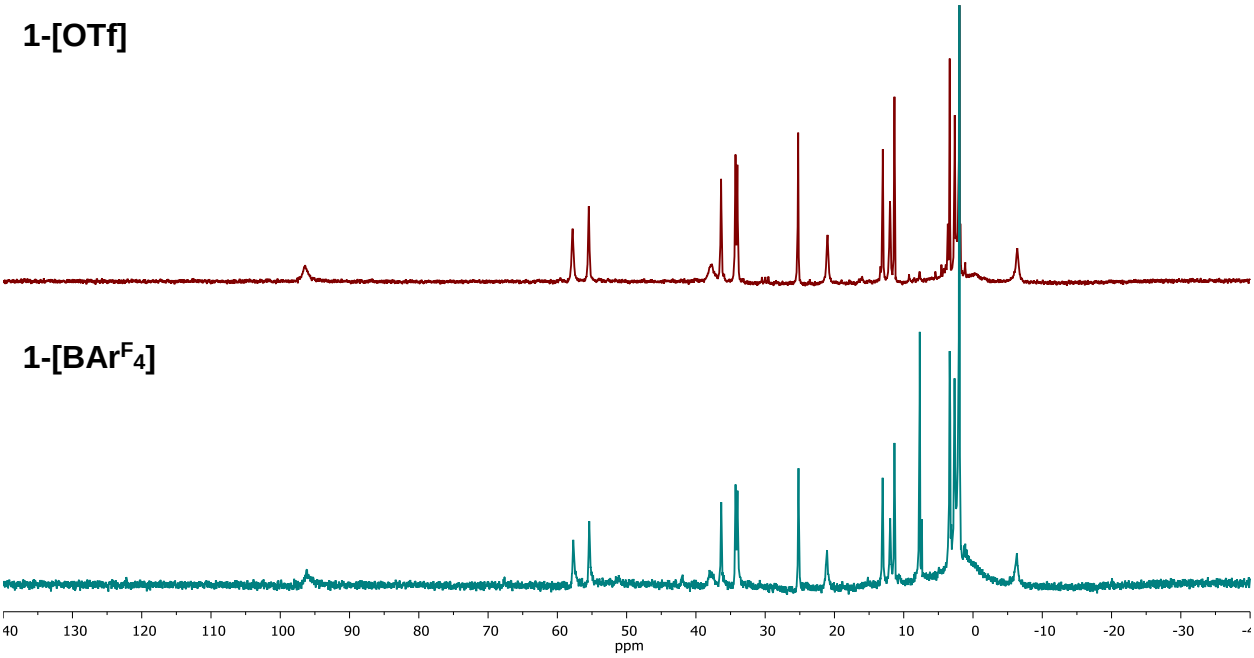

Figure S1. ^{1}H NMR spectrum (300 MHz) of [LFe$_3$O(Pz)$_3$Mn][OTf] (**1-[OTf]**) (top) and [LFe$_3$O(Pz)$_3$Mn][[BArF4]] (**1-[BAr$^{F}_{4}$]**; bottom) in CD$_3$CN.

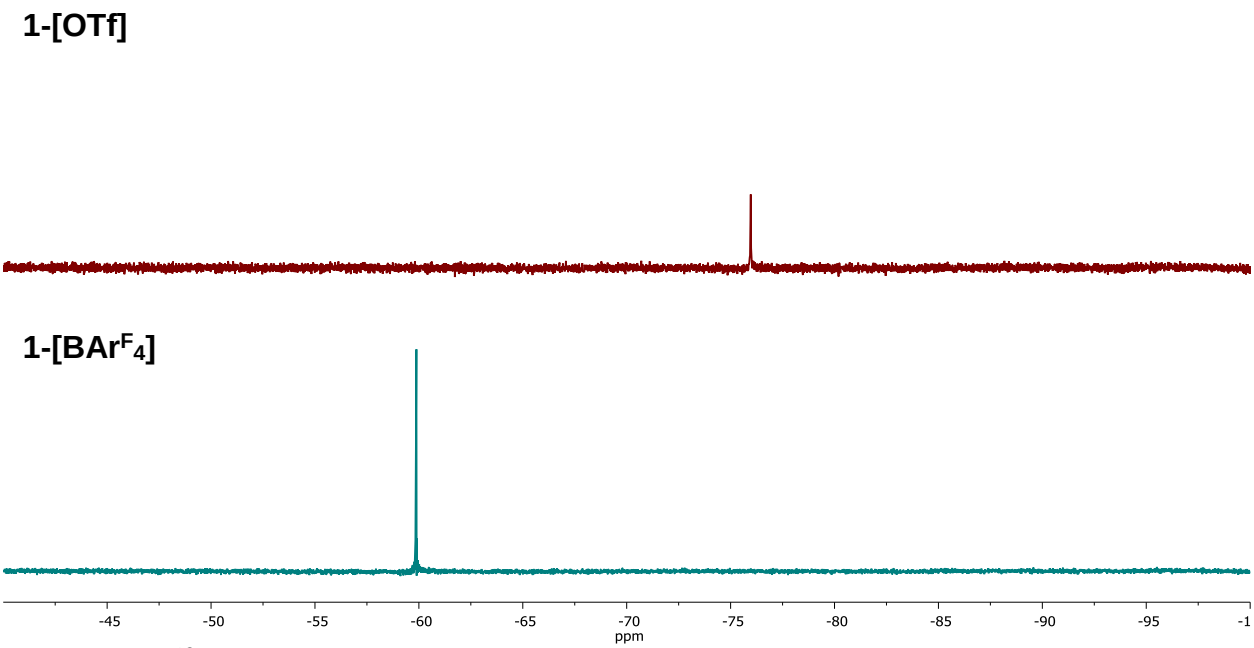

Figure S2. ^{19}F NMR spectrum (300 MHz) of [LFe$_3$O(Pz)$_3$Mn][OTf] (**1-[OTf]**; top) and [LFe$_3$O(Pz)$_3$Mn][BAr$^{F}_{4}$] (**1-[BAr$^{F}_{4}$]**; bottom) in CD$_3$CN.

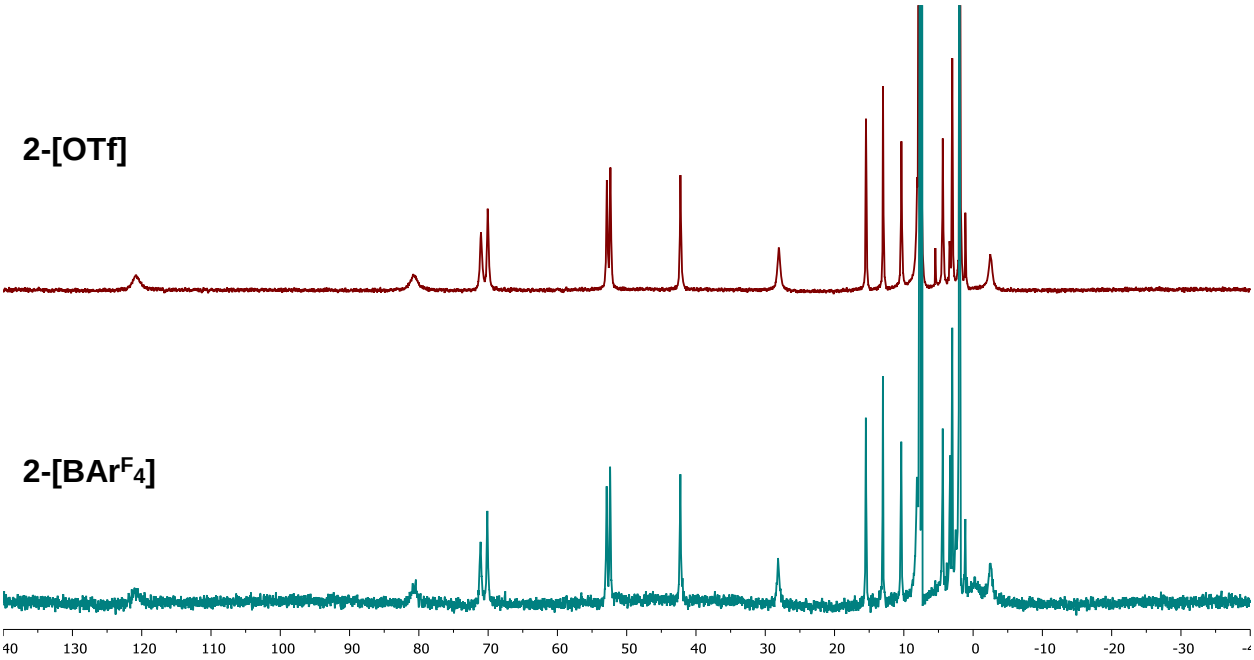

Figure S3. ^{1}H NMR spectrum (300 MHz) of $[LFe_3O(Pz)_3Mn][OTf]_2$ (**2-[OTf]**; top) and $[LFe_3O(Pz)_3Mn][BAr^F{}_4]_2$ (**2-[BAr$^{F}_{4}$]**; bottom) in CD_3CN.

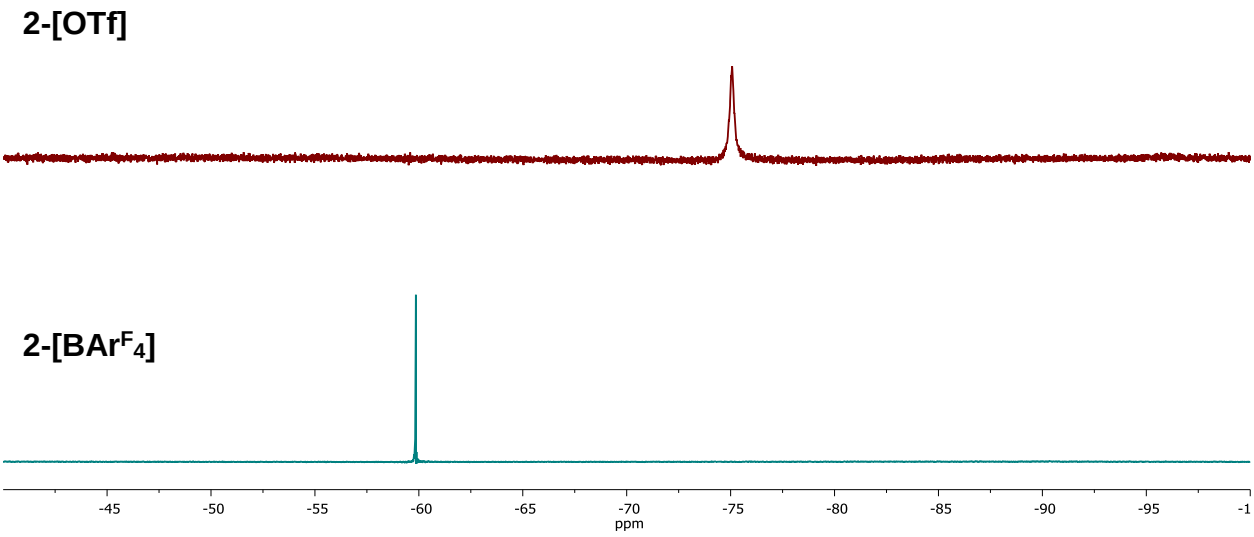

Figure S4. ^{19}F NMR spectrum (300 MHz) of $[LFe_3O(Pz)_3Mn][OTf]_2$ (**2-[OTf]**; top) and $[LFe_3O(Pz)_3Mn][BAr^F{}_4]_2$ (**2-[BAr$^{F}_{4}$]**; bottom) in CD_3CN.

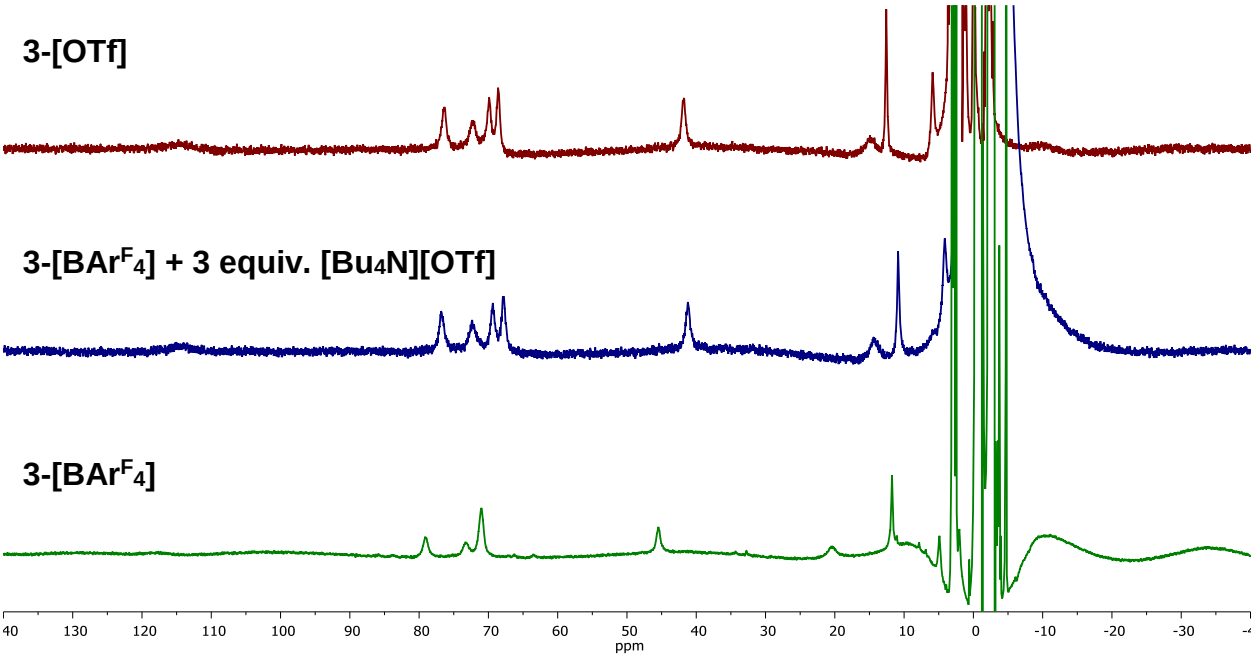

Figure S5. ^{1}H NMR spectrum (300 MHz) of $[LFe_3O(Pz)_3Mn][OTf]_3$ in CD_2Cl_2 (**3-[OTf]**; top), $[LFe_3O(Pz)_3Mn][BAr^F{}_4]_3$ in THF/C_6D_6 with three equivalents tetrabutylammonium trifluoromethanesulfonate (500 MHz, middle), and $[LFe_3O(Pz)_3Mn][BAr^F{}_4]_3$ in THF/C_6D_6 (500 MHz) (**3-[BArF4]**; bottom).

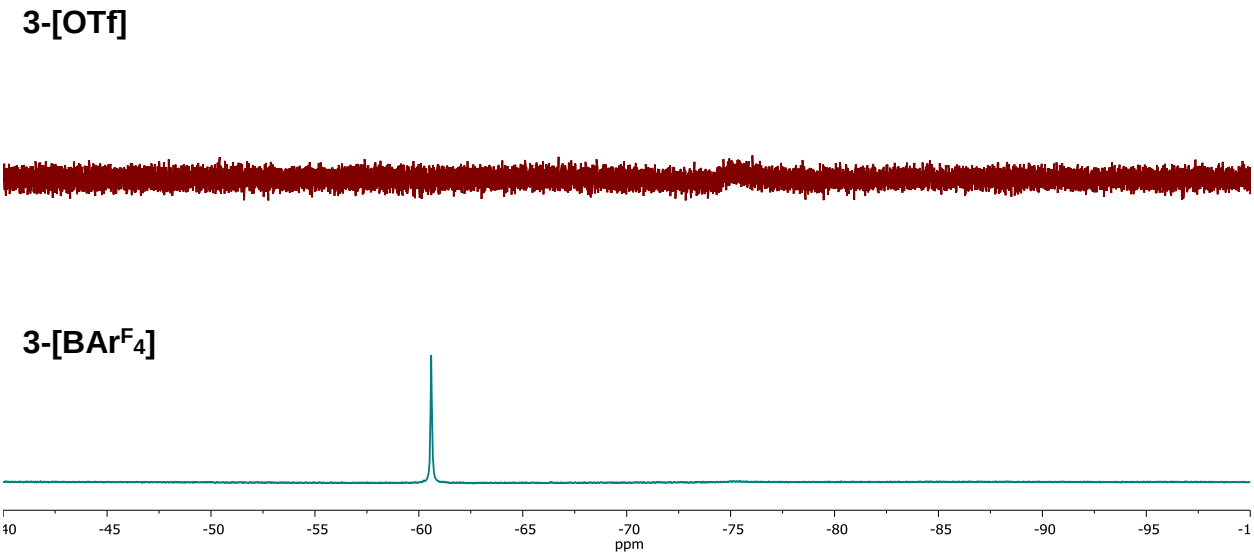

Figure S6. ^{19}F NMR spectrum (300 MHz) of $[LFe_3O(Pz)_3Mn][OTf]_3$ (**3-[OTf]**) in CD_2Cl_2 (top) and $[LFe_3O(Pz)_3Mn][BAr^F{}_4]_3$ (**3-[BArF4]**; bottom) in THF/C_6D_6 (500 MHz).

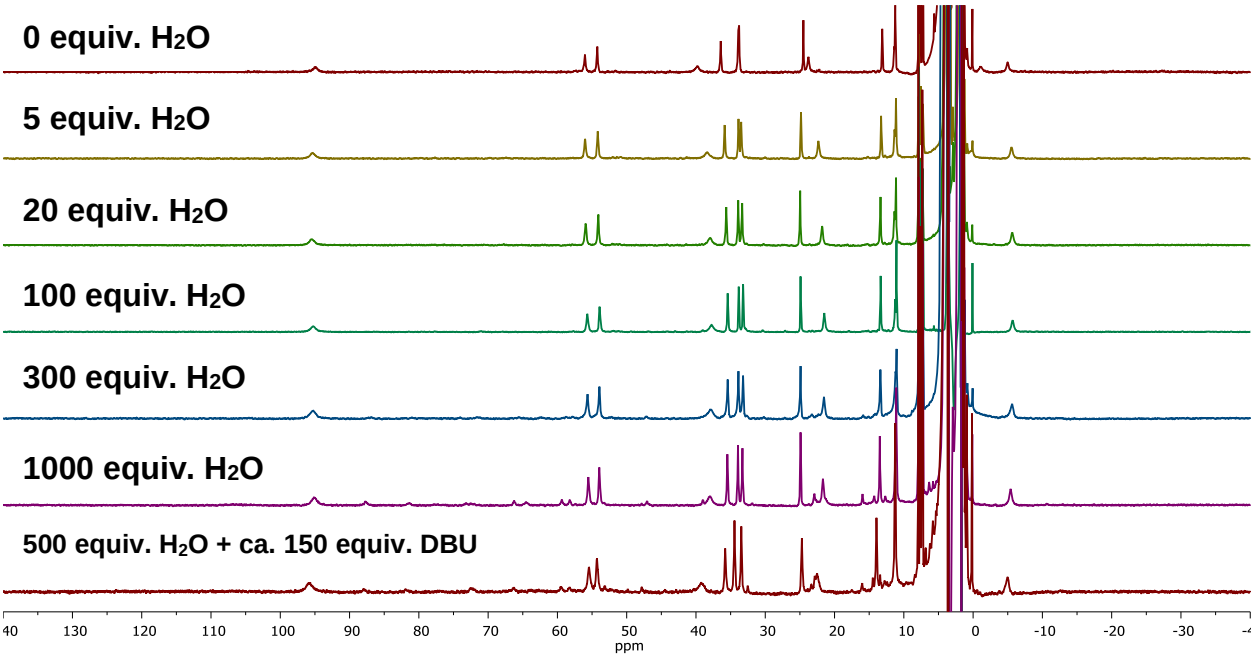

Figure S7. ^{1}H NMR spectra (500 MHz) of 2mM [$LFe_3O(Pz)_3Mn$][BAr^F_4] (**1-[BAr^F_4]**) in THF/C_6D_6 with various equivalents of H_2O. Splitting of the peak at ~35 ppm was used to judge the amount of H_2O coordination, which appeared complete at > 20 equivalents H_2O. Addition of excess 1,8-diazabicyclo(5.4.0)undec-7-ene (DBU) leads to no significant change in the ^{1}H NMR spectrum.

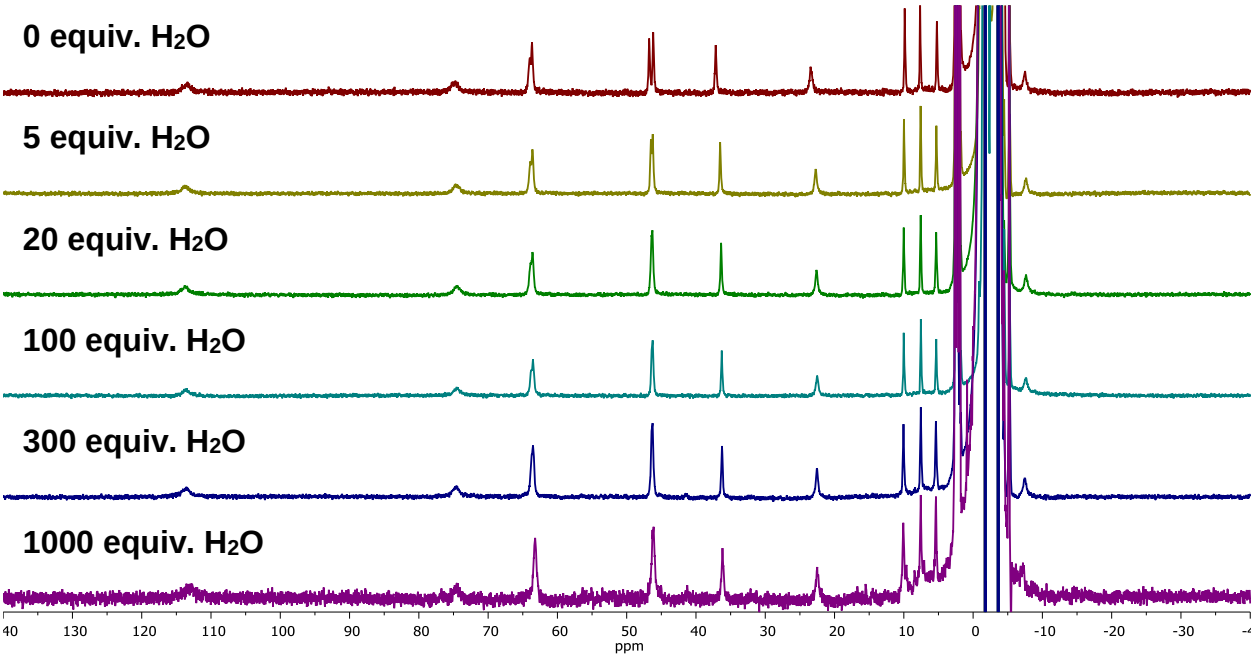

Figure S8. ^{1}H NMR spectra (500 MHz) of 2mM [$LFe_3O(Pz)_3Mn$][BAr^F_4]$_2$ (**2-[BAr^F_4]**) in THF/C_6D_6 with various equivalents of H_2O. Coalescence of the two peaks at ~45 ppm was used to judge the amount of H_2O coordination, which appeared complete at > 20 equivalents H_2O.

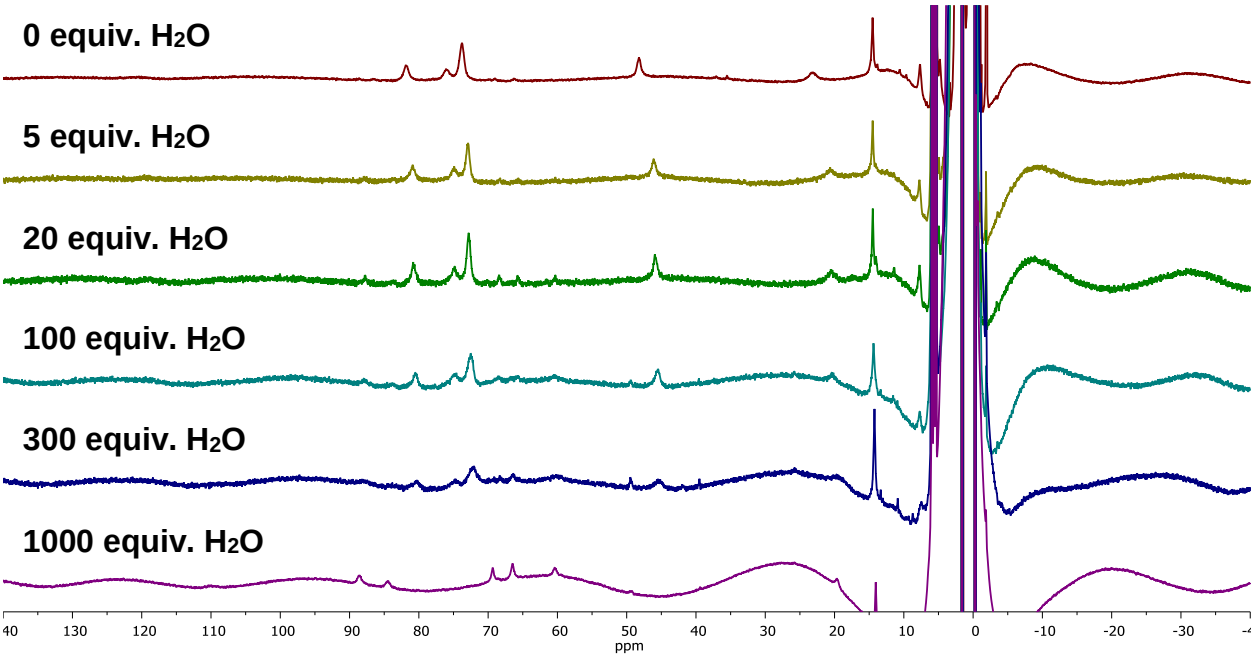

Figure S9. ^{1}H NMR spectra (500 MHz) of $[LFe_3O(Pz)_3Mn][BAr^F{}_4]_3$ (**3-[BAr$^F{}_4$]**) in THF/C_6D_6 with various equivalents of H_2O. The upfield shift of the peak at ~50 ppm was used to judge the amount of H_2O coordination, which appeared complete at > 20 equivalents H_2O.

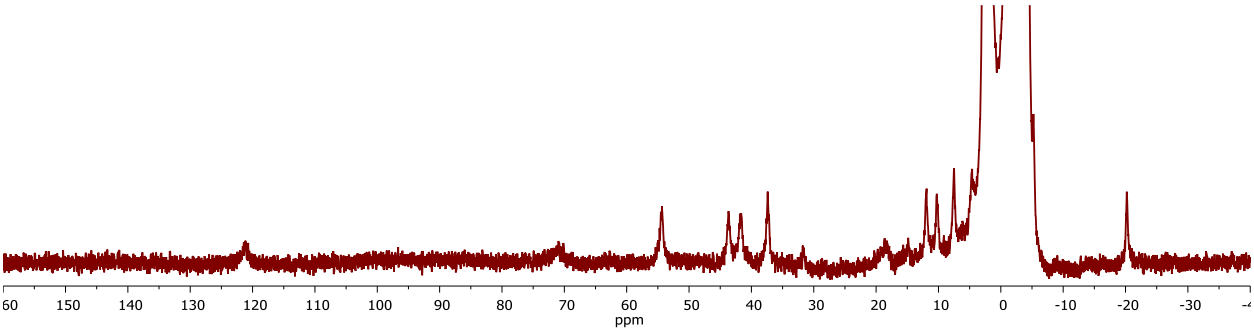

Figure S10. ^{1}H NMR spectra (500 MHz) of $[LFe_3O(Pz)_3Mn(OH)]$ (**5**) in THF/C_6D_6 [250 mM H_2O].

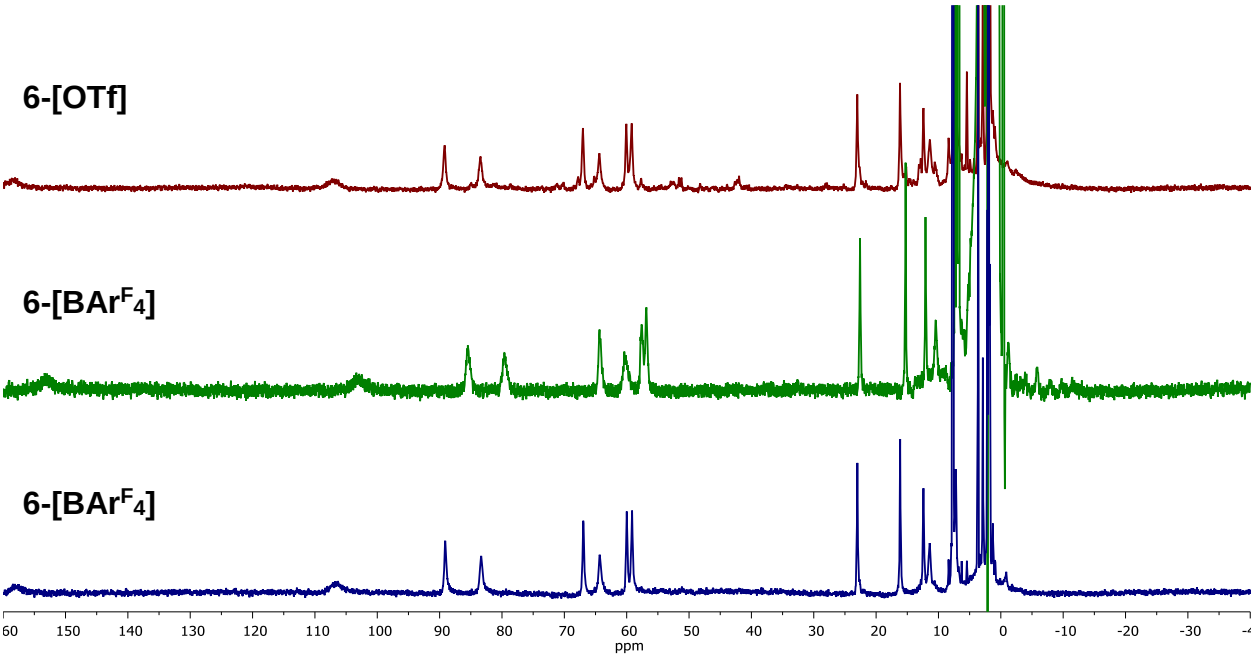

Figure S11. ^{1}H NMR spectrum (300 MHz) of [LFe$_3$O(Pz)$_3$Mn(OH)][OTf] (**6-[OTf]**; top) and [LFe$_3$O(Pz)$_3$Mn(OH)][BAr$^{F}_{4}$] (**6-[BAr$^{F}_{4}$]**; middle) in CD3CN. ^{1}H NMR spectrum (500 MHz) of [LFe$_3$O(Pz)$_3$Mn(OH)][BAr$^{F}_{4}$] (**6-[BAr$^{F}_{4}$]**; bottom) in THF/C$_6$D$_6$ [250 mM H$_2$O].

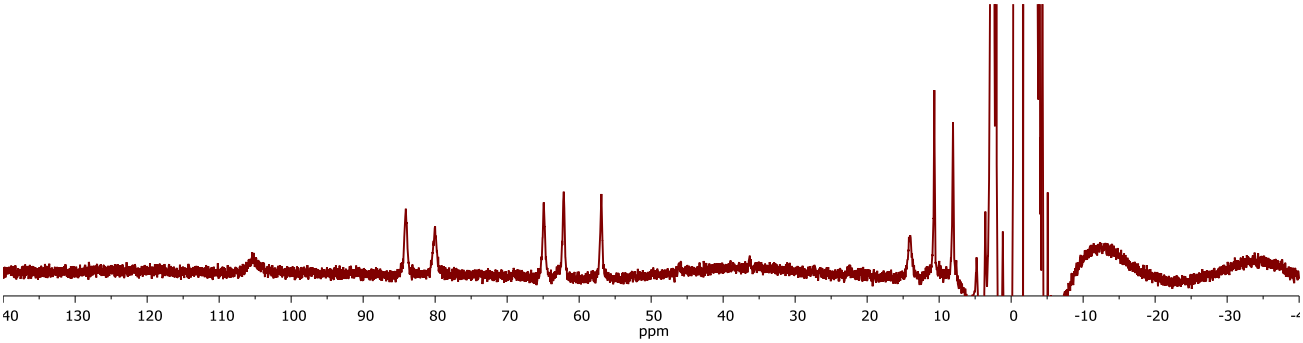

Figure S12. ^{1}H NMR spectrum (500 MHz) of [LFe$_3$O(Pz)$_3$Mn(OH)][BAr$^{F}_{4}$]$_2$ (**7-[BAr$^{F}_{4}$]**) in THF/C$_6$D$_6$ [250 mM H$_2$O].

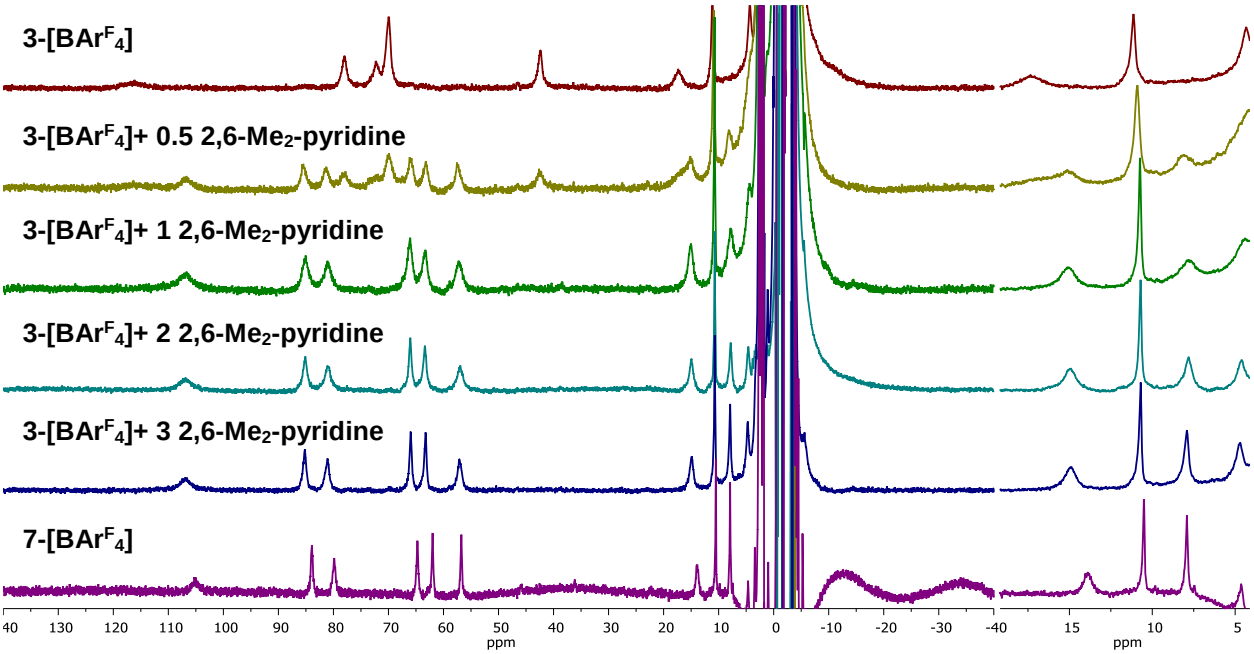

Figure S13. ^{1}H NMR spectrum (500 MHz) of $[LFe_3O(Pz)_3Mn][BAr^F{}_4]_3$ (**3-[BAr$^F{}_4$]**) with various equivalents of 2,6-dimethyl-pyridine in THF/C_6D_6 [250 mM H_2O].

^{1}H NMR	δ (ppm)	$X_{\mathbf{3\text{-}[BArF4]}}$	K
3-[BAr$^F{}_4$]	11.12	-	
3-[BAr$^F{}_4$] + 0.5 2,6-Me$_2$-Py	10.90	0.632	1.625
3-[BAr$^F{}_4$] + 1 2,6-Me$_2$-Py	10.72	0.343	3.661
3-[BAr$^F{}_4$] + 2 2,6-Me$_2$-Py	10.70	0.319	1.100
3-[BAr$^F{}_4$] + 3 2,6-Me$_2$-Py	10.69	0.296	0.730
7-[BAr$^F{}_4$]	10.51	-	
		Average K	1.779 (±0.654)

Table S1. pK_a titration of **3-[BAr$^F{}_4$]** via ^{1}H NMR spectroscopy with 2,6-dimethyl-pyridine. A sharp resonance ~ 11 ppm was selected to measure the mole fraction of **3-[BAr$^F{}_4$]** ($X_{\mathbf{3\text{-}[BArF4]}}$), as **3-[BAr$^F{}_4$]** and **7-[BAr$^F{}_4$]** undergo fast exchange on the NMR time-scale. The concentrations of **3-[BAr$^F{}_4$]**, 2,6-Me$_2$-Py, and [2,6-Me$_2$-PyH][BAr$^F{}_4$] were determined from $X_{\mathbf{3\text{-}[BArF4]}}$ via mass balance. These values were used to calculate the proton transfer equilibrium constant, K, according to the equation below:

$$K = \frac{[\mathbf{7}-[\mathbf{BAr^F_4}]][(2{,}6-\mathrm{Me_2}-\mathrm{PyH})([\mathrm{BAr^F_4}])]}{[\mathbf{3}-[\mathbf{BAr^F_4}]][2{,}6-\mathrm{Me_2}-\mathrm{Py}]}$$

This value, along with the reported pK_a of [2,6-Me2-Py]$^+$, 9.5,[8] was used to obtain the pK_a value of 9.2 for **3-[BAr$^F{}_4$].**

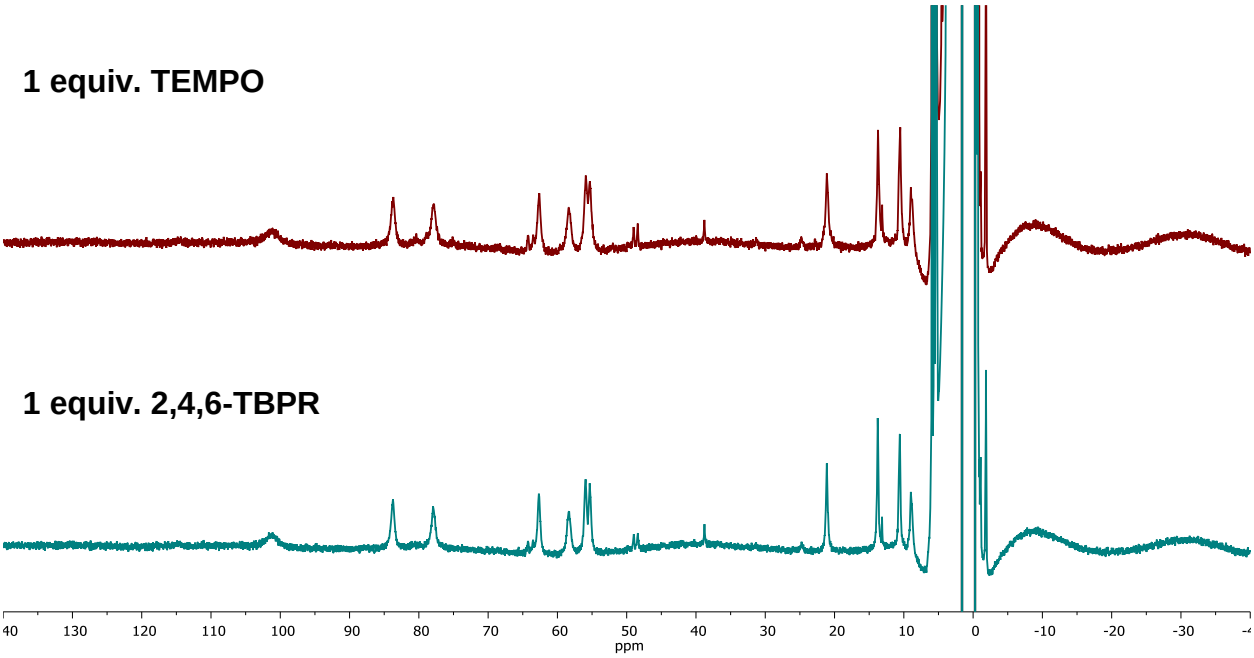

Figure S14. ^{1}H NMR spectrum (500 MHz) of 2mM [$LFe_3O(Pz)_3Mn$][BAr^F_4] (**1-[BAr^F_4]**) in THF/C_6D_6 [250 mM H_2O] in the presence of 1 equivalent TEMPO (top) and 2,4,6-tri-tert-butylphenoxy radical (bottom). The major species of both NMRs matches the NMR of the [$LFe_3O(Pz)_3Mn(OH)$][BAr^F_4] cluster (**6-[BAr^F_4]**).

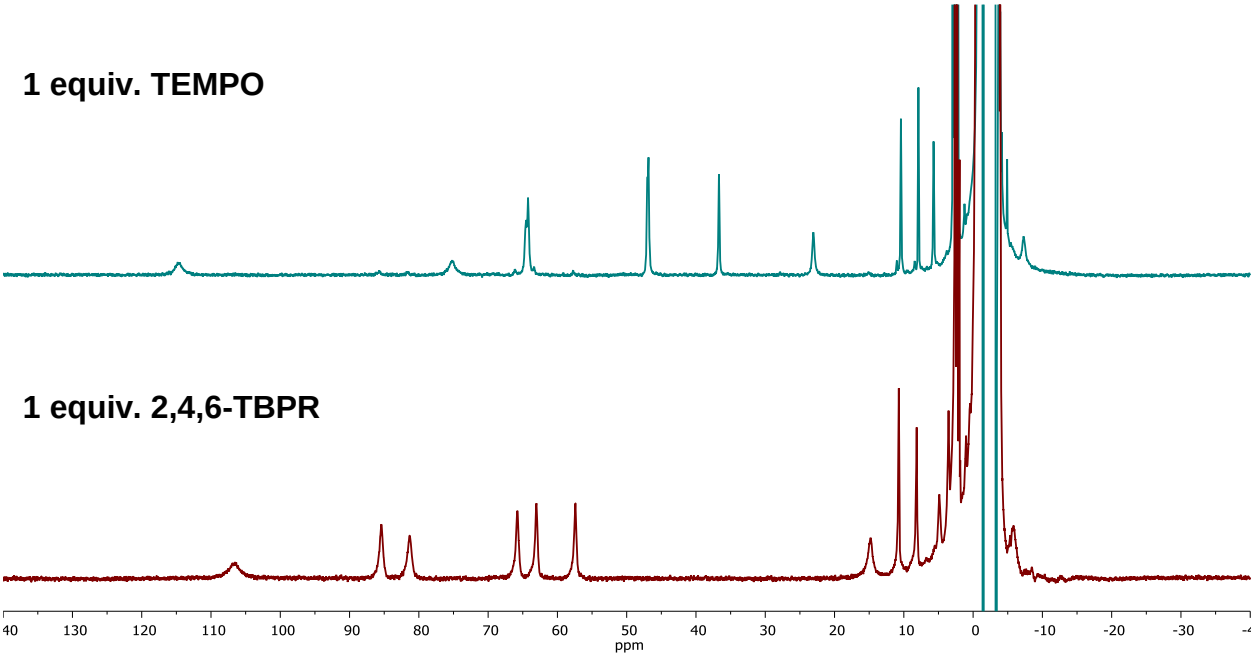

Figure S15. ^{1}H NMR spectrum (500 MHz) of 2mM [$LFe_3O(Pz)_3Mn$][BAr^F_4]$_2$ (**2-[BAr^F_4]**) in THF/C_6D_6 [250 mM H_2O] in the presence of 1 equivalent TEMPO (top) and 2,4,6-tri-tert-butylphenoxy radical (bottom). The the top NMR corresponds to starting material, **2-[BAr^F_4]**, while the bottom NMR corresponds to the [$LFe_3O(Pz)_3Mn(OH)$][BAr^F_4]$_2$ cluster (**7-[BAr^F_4]**).

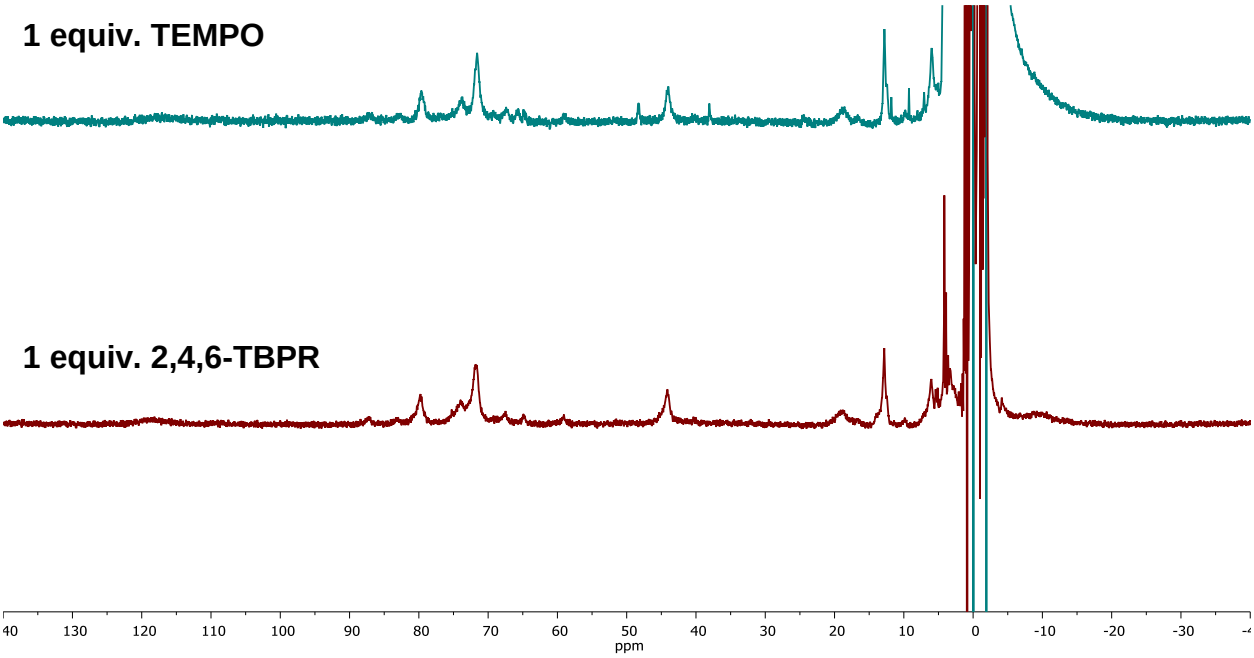

Figure S16. ^{1}H NMR spectrum (500 MHz) of 2mM $[LFe_3O(Pz)_3Mn][BAr^F{}_4]_3$ (**3-[BAr$^F{}_4$]**) in THF/C_6D_6 [250 mM H_2O] in the presence of 1 equivalent TEMPO (top) and 2,4,6-tri-tert-butylphenoxy radical (bottom). The major species of both NMRs corresponds to starting material (**3-[BAr$^F{}_4$]**).

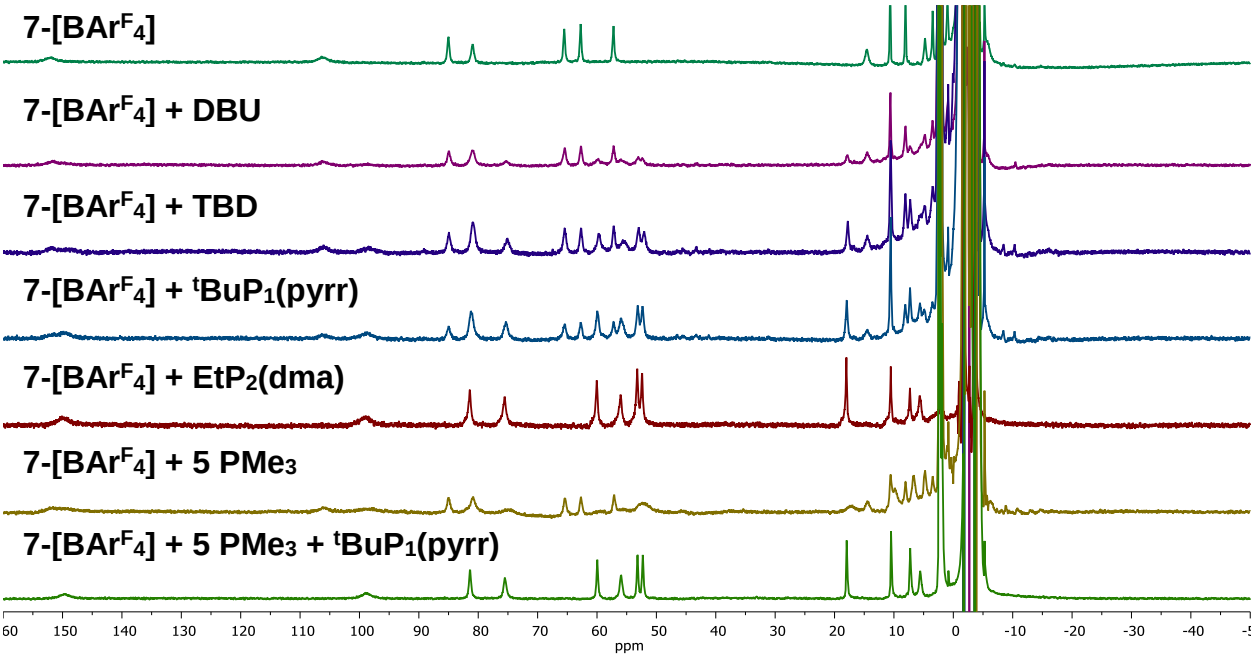

Figure S17. ^{1}H NMR spectra (500 MHz) of 2mM $[LFe_3O(Pz)_3Mn(OH)][BAr^F{}_4]_2$ (**7-[BAr$^F{}_4$]**) in THF/C_6D_6 [250 mM H_2O] in the presence of 1 equivalent various bases or with 5 equivalents trimethylphosphine and '^{t}BuP$_1$(pyrr)' base. Addition of each base produces, in varying amounts, a spectrum that matches the NMR of the one electron reduced cluster, $[LFe_3O(Pz)_3Mn(OH)][BAr^F{}_4]$ (**6-[BAr$^F{}_4$]**).

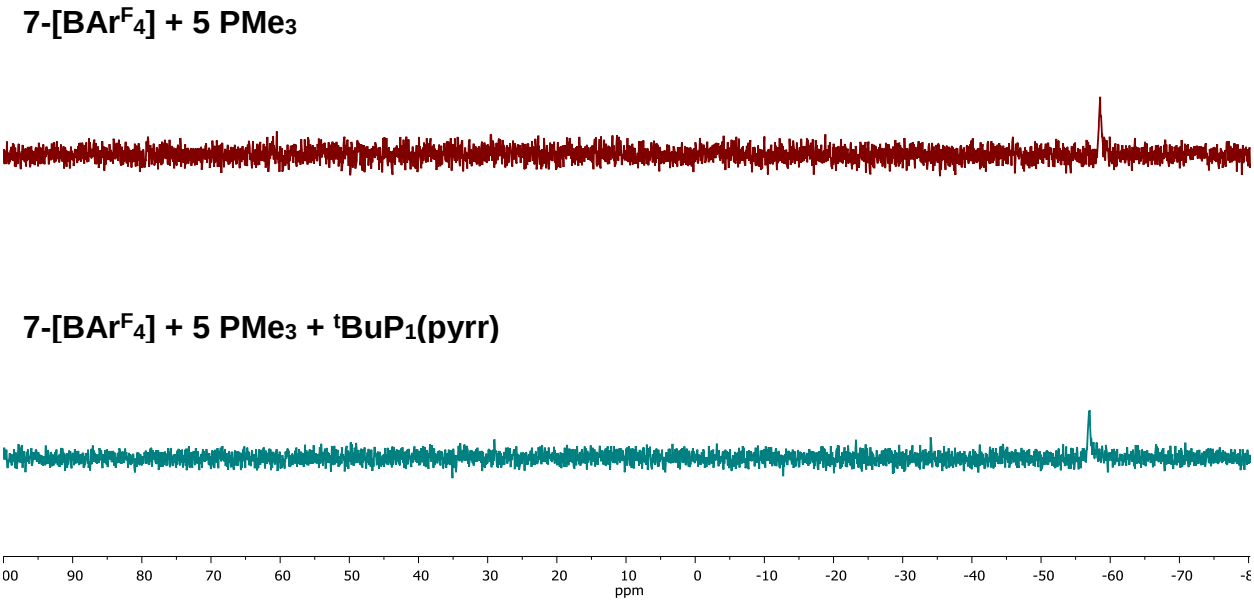

Figure S18. ^{31}P NMR spectra (120 MHz) of 2mM $[LFe_3O(Pz)_3Mn(OH)][BAr^F{}_4]_2$ (**7-[BAr$^F{}_4$]**) in THF/C_6D_6 [250 mM H_2O] in the presence of 5 equivalents trimethylphosphine with and without '^{t}BuP$_1$(pyrr)' base.

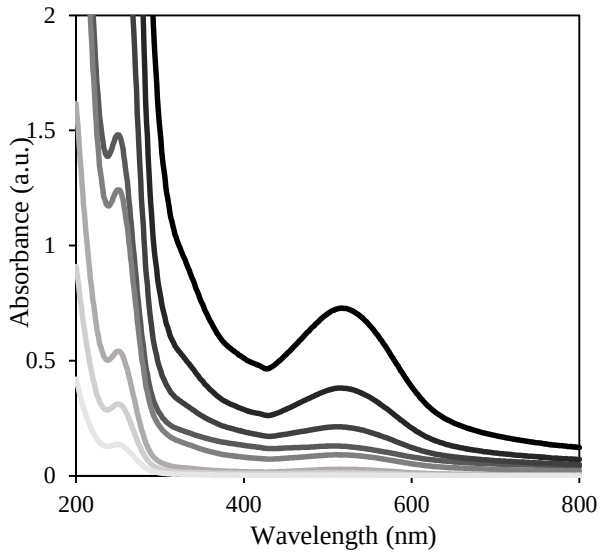

Figure S19. UV-Vis absorbance spectra of [$LFe_3O(Pz)_3Mn$][OTf] (**1-[OTf]**; 1 cm cuvette; 200, 100, 50, 25, 20, 10, 5, and 2.5 μM) in MeCN. [ε (M^{-1} cm^{-1})] 250 nm (6.08×10^4), 517 nm (3.72×10^3).

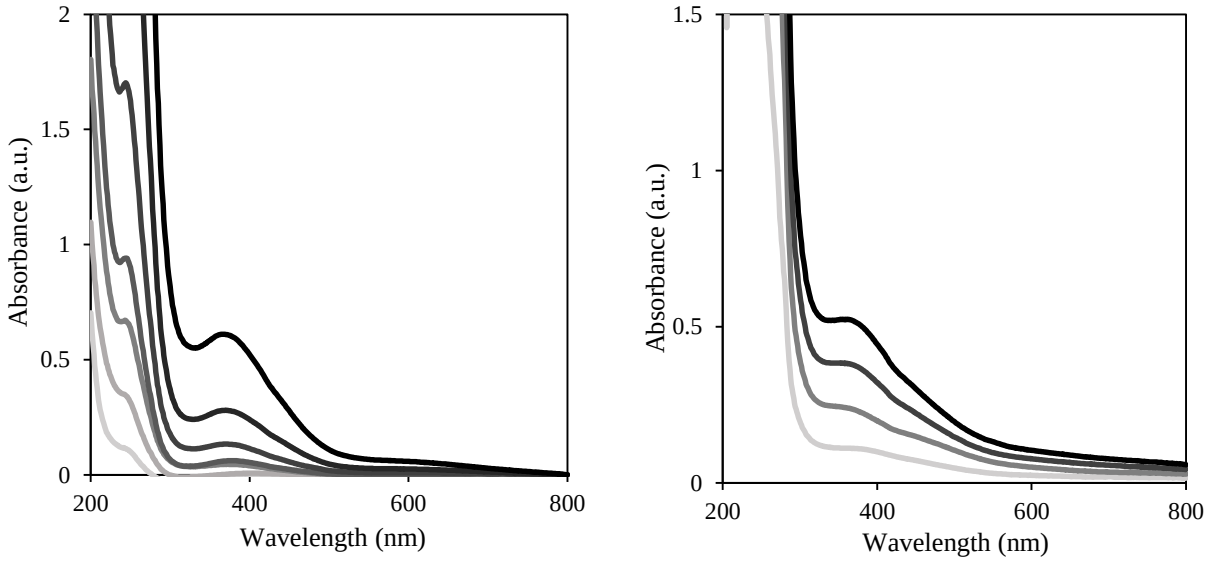

Figure S20. (Left) UV-Vis absorbance spectra of [$LFe_3O(Pz)_3Mn$][$OTf]_2$ (**2-[OTf]**; 1 cm cuvette; 100, 50, 25, 15, 10, 5, and 2.5 μM) in MeCN. [ε (M^{-1} cm^{-1})] 241 nm (6.53×10^4), 368 nm (6.49×10^3). (Right) UV-Vis absorbance spectra of [$LFe_3O(Pz)_3Mn$][$BAr^F{}_4]_2$ (**2-[$BAr^F{}_4$]**; 1 cm cuvette; 100, 75, 50, and 20 μM) in THF/250 mM H_2O. [ε (M^{-1} cm^{-1})] 368 nm (5.11×10^3).

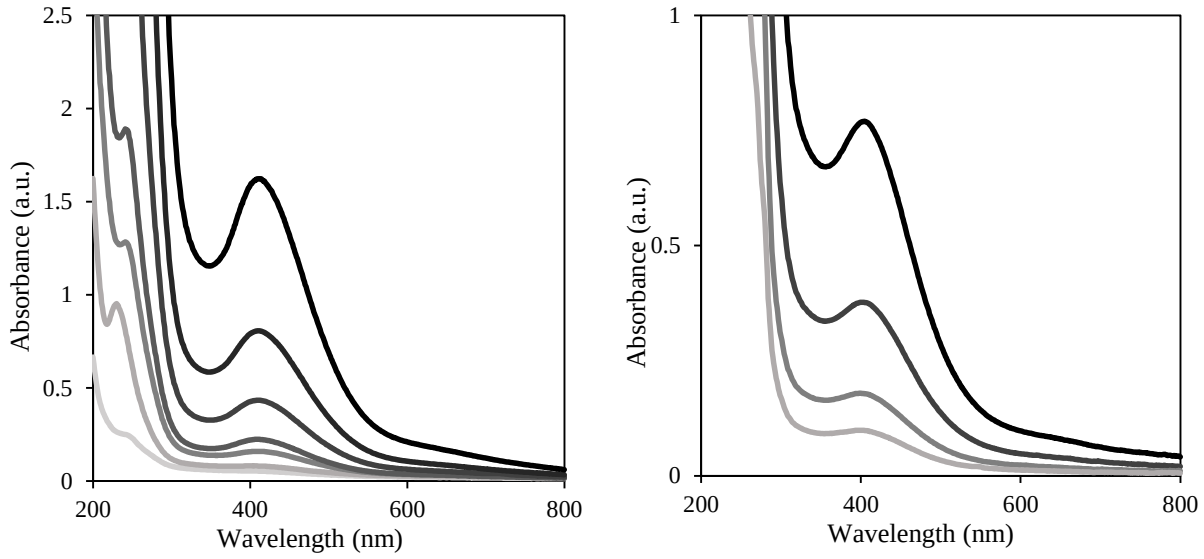

Figure S21. (Left) UV-Vis absorbance spectra of $[LFe_3O(Pz)_3Mn][OTf]_3$ (**3-[OTf]**; 1 cm cuvette; 200, 100, 50, 25, 15, 5, and 2.5 μM) in MeCN. [ε (M^{-1} cm^{-1})] 241 nm (7.84×10^4), 411 nm (9.22×10^3). (Right) UV-Vis absorbance spectra of $[LFe_3O(Pz)_3Mn][BAr^F{}_4]_3$ (**3-[BAr$^F{}_4$]**; 1 cm cuvette; 100, 50, 25, and 12.5 μM) in THF/250 mM H_2O. [ε (M^{-1} cm^{-1})] 405 nm (7.64×10^3).

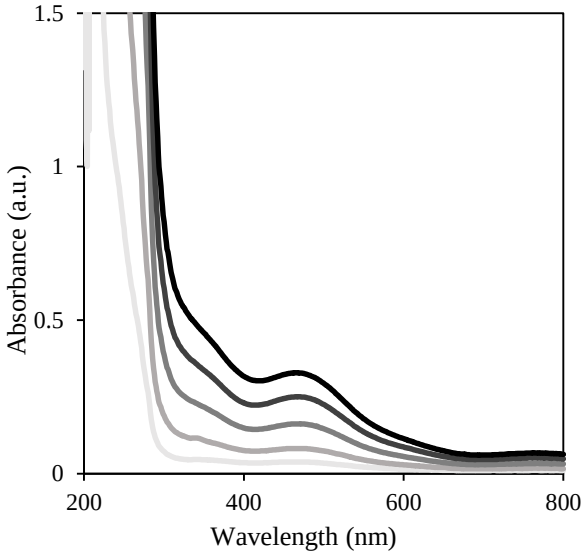

Figure S22. UV-Vis absorbance spectra of $[LFe_3O(Pz)_3Mn(OH)][BAr^F{}_4]$ (**6-[BAr$^F{}_4$]**; 1 cm cuvette; 100, 75, 50, 25, and 10 μM) in THF/250 mM H_2O. [ε (M^{-1} cm^{-1})] 467 nm (3.29×10^3).

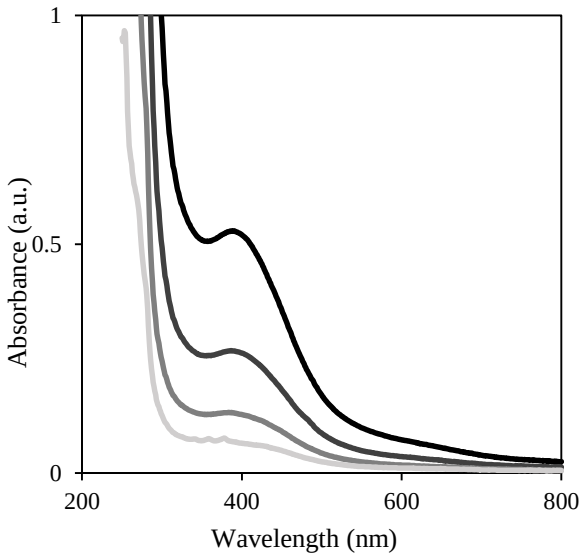

Figure S23. UV-Vis absorbance spectra of $[LFe_3O(Pz)_3Mn(OH)][BAr^F{}_4]_2$ (**7-[BAr$^F{}_4$]**; 1 cm cuvette; 100, 50, 25, and 12.5 μM) in THF/250 mM H_2O. [ε (M^{-1} cm^{-1})] 389 nm (5.29×10^3).

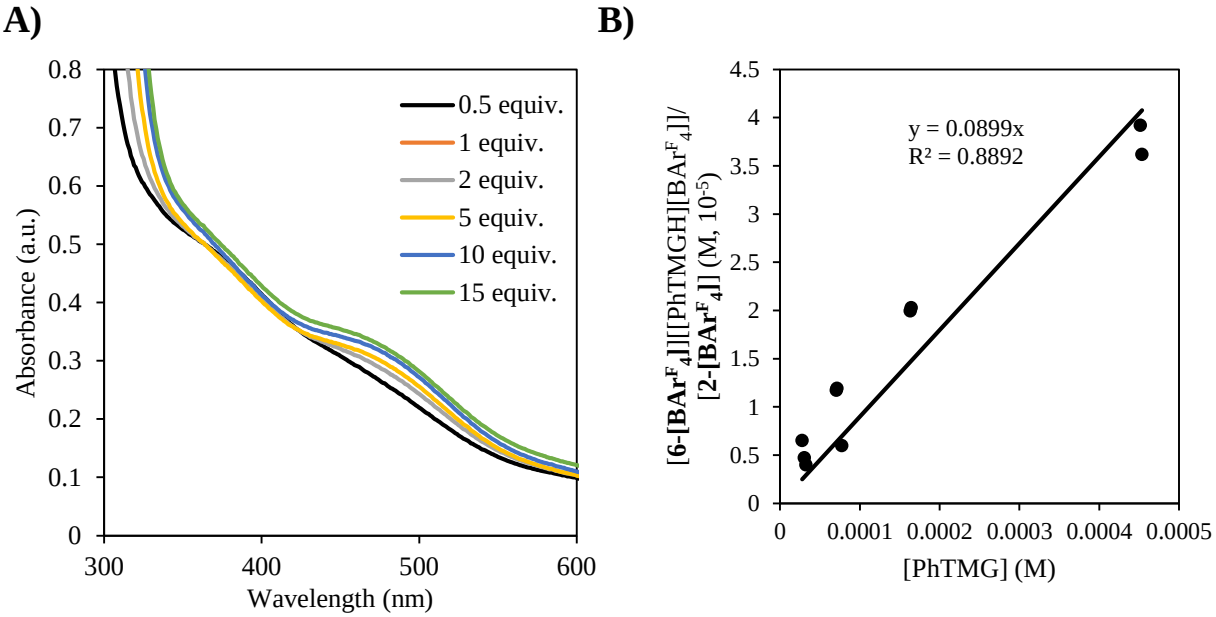

Figure S24. (A) UV-Vis absorbance spectra of $[LFe_3O(Pz)_3Mn][BAr^F{}_4]_2$ (**2-[BAr$^F{}_4$]**; 1 cm cuvette; 100μM) in THF [250 mM H_2O] after addition of various equivalents of 1,1,3,3-tetramethyl-2-phenylguanidine (PhTMG; pK_a(THF) = 16.5).[8] (B) Titration plot for deprotonation of $[LFe_3O(Pz)_3Mn][BAr^F{}_4]_2$ (**2-[BAr$^F{}_4$]**) to $[LFe_3O(Pz)_3Mn(OH)][BAr^F{}_4]$ (**6-[BAr$^F{}_4$]**) based on multiple titrations; the slope of the line represents an equilibrium constant value of K = 0.09, where:

$$K = \frac{[\mathbf{6}\text{–}[\mathbf{BAr^F_4}]][(\text{PhTMGH})([BAr^F_4])]}{[\mathbf{2}\text{–}[\mathbf{BAr^F_4}]][\text{PhTMG}]}$$

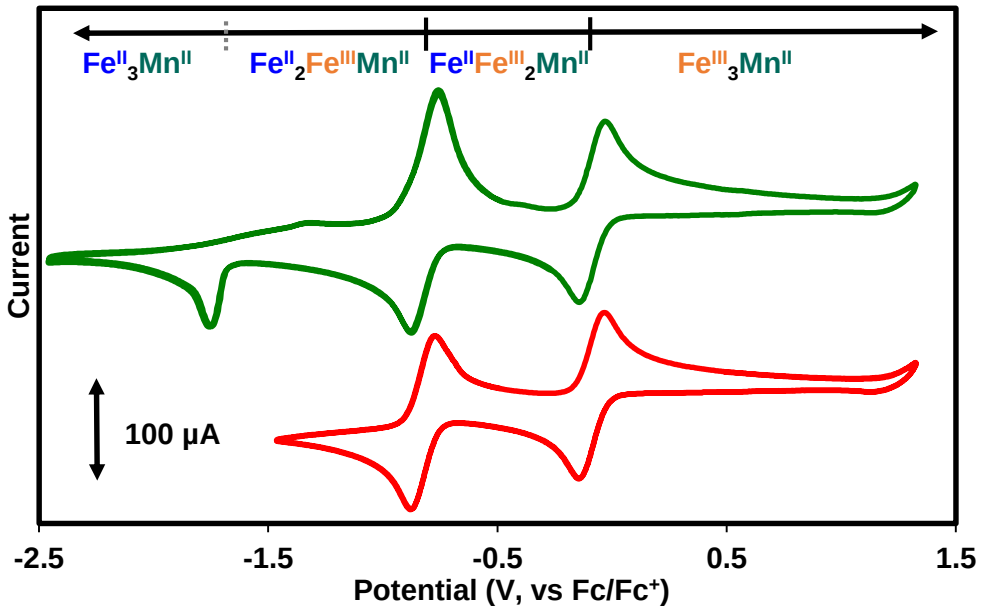

Figure S25. Cyclic voltammogram (green trace) of $[LFe_3O(Pz)_3Mn][OTf]_2$ (**2-[OTf]**, 2.8 mM) in MeCN and 100 mM $[Bu_4N][PF_6]$ at a scan rate of 200 mV/s with glassy carbon, Pt-wire, and Ag-wire as working, counter, and reference electrode, respectively. The open circuit potential was -0.5 V. (Red trace) Partial CV of **2-[OTf]** of the reversible electrochemical features.

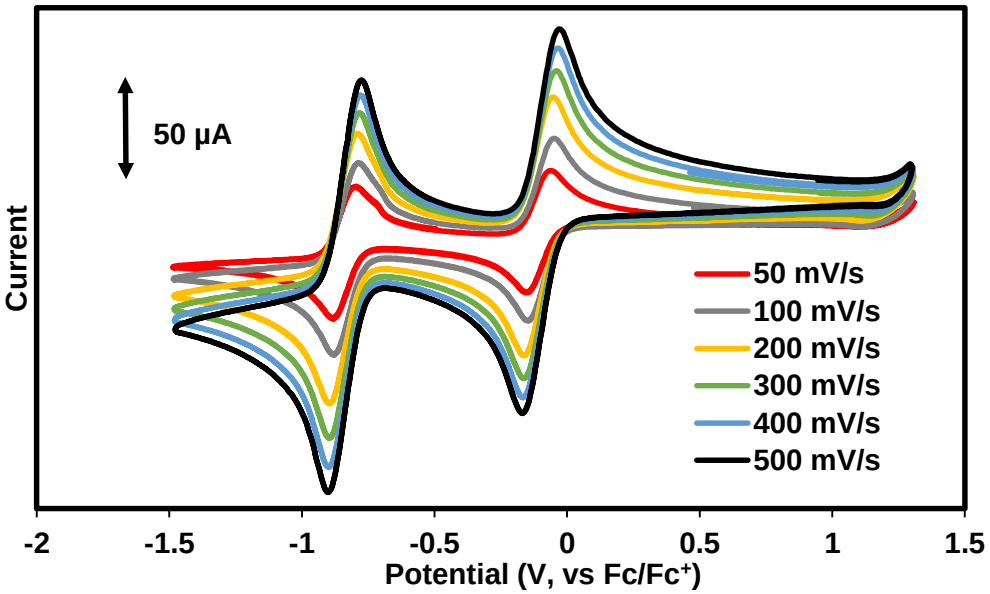

Figure S26. Cyclic voltammograms of $[LFe_3O(Pz)_3Mn][OTf]_2$ (**2-[OTf]**, 2.8 mM) in MeCN and 100 mM $[Bu_4N][PF_6]$ at various scan rates with glassy carbon, Pt-wire, and Ag-wire as working, counter, and reference electrode, respectively.

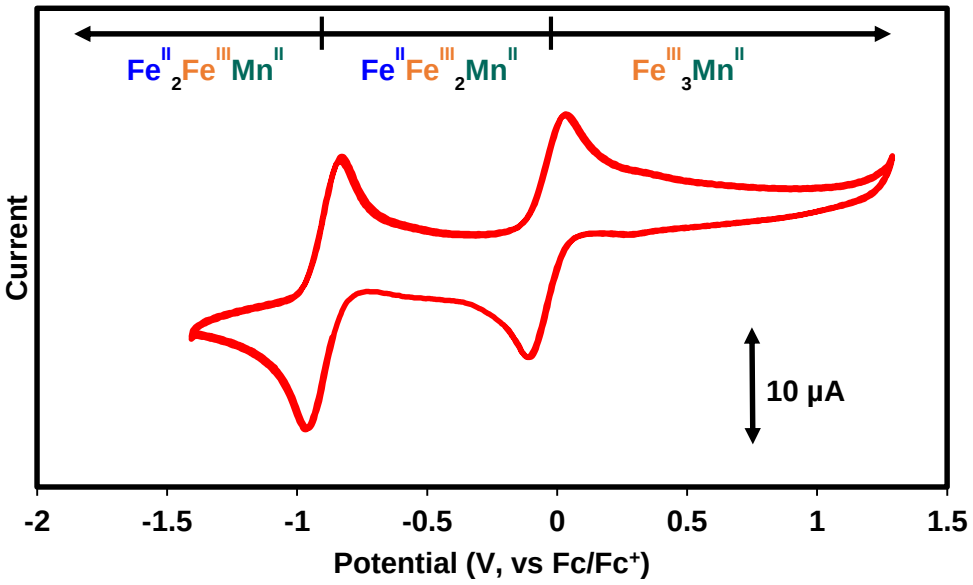

Figure S27. Cyclic voltammogram (red trace) of $[LFe_3O(Pz)_3Mn(OH_2)][BAr^F{}_4]_2$ (**2-[BAr$^F{}_4$]**, 2.1 mM) in THF [250 mM H_2O] and 100 mM $[^nPr_4N][BAr^F{}_4]$ at a scan rate of 50 mV/s with glassy carbon, Pt-wire, and Ag-wire as working, counter, and reference electrode, respectively. The open circuit potential was -0.2 V.

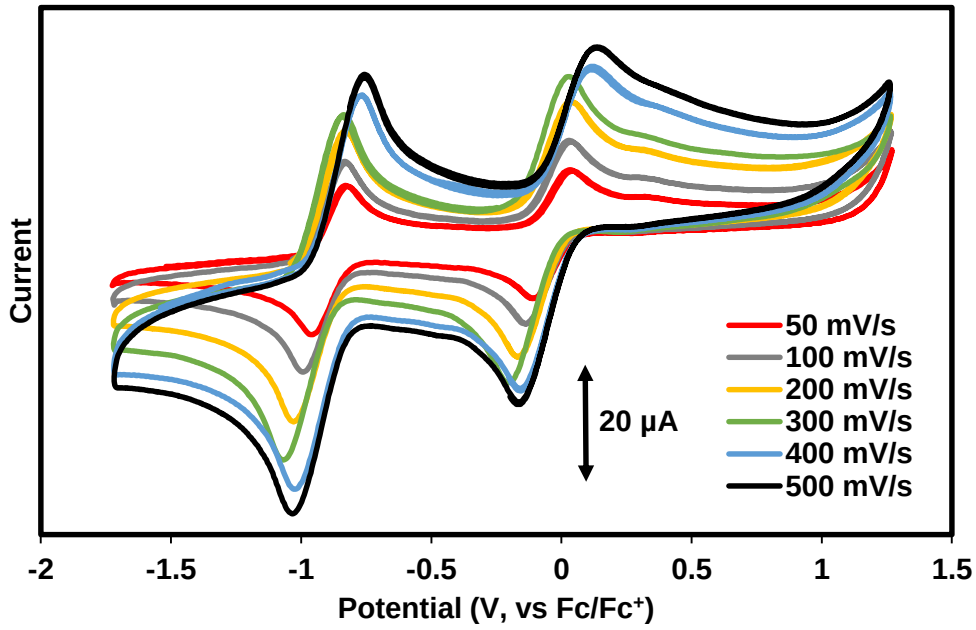

Figure S28. Cyclic voltammograms of $[LFe_3O(Pz)_3Mn(OH_2)][BAr^F{}_4]_2$ (**2-[BAr$^F{}_4$]**, 2.1 mM) in THF [250 mM H_2O] and 100 mM $[^nPr_4N][BAr^F{}_4]$ at various scan rates with glassy carbon, Pt-wire, and Ag-wire as working, counter, and reference electrode, respectively.

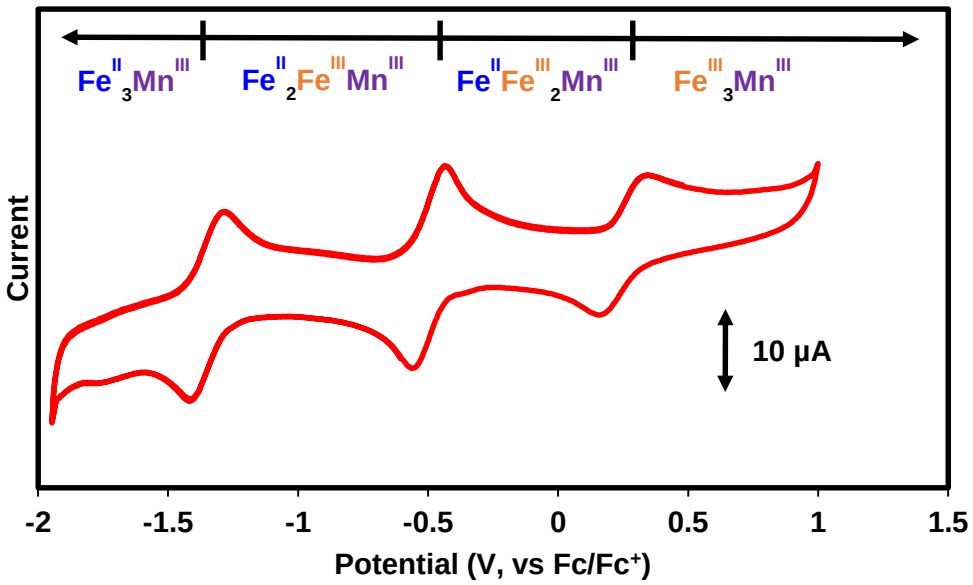

Figure S29. Cyclic voltammogram (red trace) of $[LFe_3O(Pz)_3Mn(OH)][BAr^F{}_4]$ (**6-[BAr$^F{}_4$]**, 2 mM) in THF [250 mM H_2O] and 100 mM $[^nPr_4N][BAr^F{}_4]$ at a scan rate of 50 mV/s with glassy carbon, Pt-wire, and Ag-wire as working, counter, and reference electrode, respectively. The open circuit potential was -1.0 V.

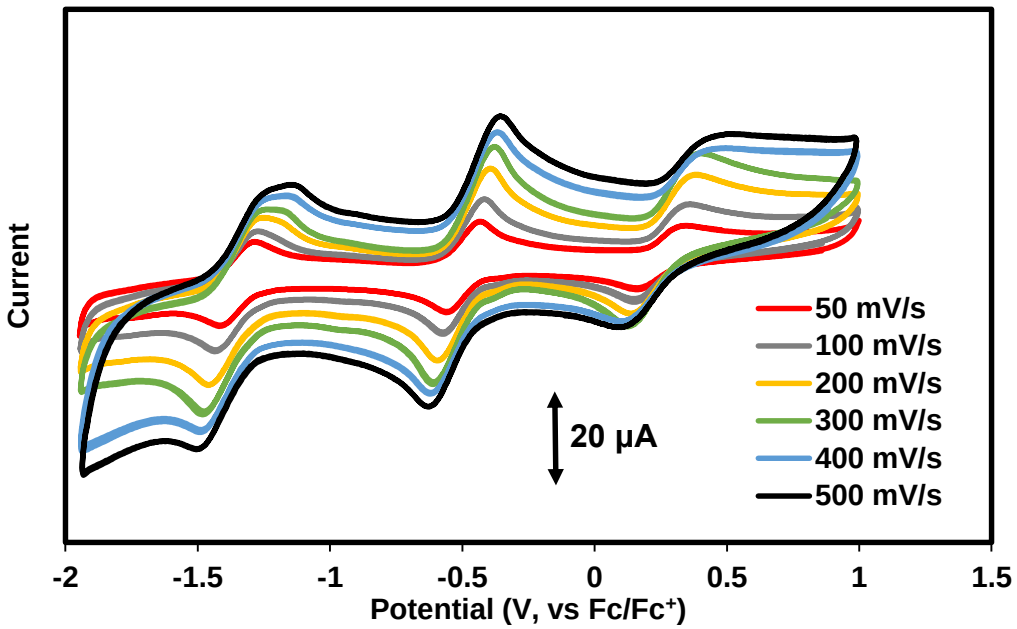

Figure S30. Cyclic voltammograms of $[LFe_3O(Pz)_3Mn(OH)][BAr^F{}_4]$ (**6-[BAr$^F{}_4$]**, 2 mM) in THF [250 mM H_2O] and 100 mM $[^nPr_4N][BAr^F{}_4]$ at various scan rates with glassy carbon, Pt-wire, and Ag-wire as working, counter, and reference electrode, respectively.

Redox Couple Assignment	E_{pa} (mV)	E_{pc}(mV)	ΔE_p(mV)	A_a (μW)	A_c (μW)	A_a/A_p
2-[OTf]						
$[Fe^{II}_2Fe^{III}Mn^{II}] \rightarrow [Fe^{II}Fe^{III}_2Mn^{II}]$	-882	-799	83	22.0	18.5	1.2
$[Fe^{II}Fe^{III}_2Mn^{II}] \rightarrow [Fe^{III}_3Mn^{II}]$	-154	-66	88	11.4	12.2	0.9
2-[BAr$^F_4$]						
$[Fe^{II}_2Fe^{III}Mn^{II}] \rightarrow [Fe^{II}Fe^{III}_2Mn^{II}]$	-958	-831	127	7.9	2.8	2.8
$[Fe^{II}Fe^{III}_2Mn^{II}] \rightarrow [Fe^{III}_3Mn^{II}]$	-93	44	137	2.6	2.5	1.0
6-[BAr$^F_4$]						
$[Fe^{II}_3Mn^{III}] \rightarrow [Fe^{II}_2Fe^{III}Mn^{III}]$	-1,406	-1,274	132	6.6	2.6	2.5
$[Fe^{II}_2Fe^{III}Mn^{III}] \rightarrow [Fe^{II}Fe^{III}_2Mn^{III}]$	-548	-426	122	4.2	3.6	1.2
$[Fe^{II}Fe^{III}_2Mn^{III}] \rightarrow [Fe^{III}_3Mn^{III}]$	172	354	182	1.6	3.0	0.5

Table S2. Peak-to-peak separation (ΔE_p; mV) and peak area ratio ($A_{a/c}$) for the redox couples in **2-[OTf]**, **2-[BAr$^F_4$]**, and **6-[BAr$^F_4$]**.

Electrochemistry Data for Constructing the Potential – pK_a Diagram of [$LFe_3O(Pz)_3Mn(OH_x)$] Clusters. Cyclic voltammetry was performed on ~2 mM solutions of $[LFe_3O(Pz)_3Mn][BAr^F{}_4]_2$ (**2-[$BAr^F{}_4$]**), or $[LFe_3O(Pz)_3Mn(OH)][BAr^F{}_4]$ (**6-[$BAr^F{}_4$]**) with glassy carbon working, Pt wire counter, and Ag wire reference electrodes in THF [250 mM H_2O] and ca. 100 mM $[^nPr_4N][BAr^F{}_4]$. After collecting a blank CV, and CV of the cluster, one equivalent of a base was added by injecting a concentrated solution of it to the cluster solution and mixing via pipette. It was observed that quasi-reversible waves corresponding to PCET could be observed best at slow scan rates (< 200 mV/s) for all bases tested; faster scan rates led to loss of a return wave for the PCET. We postulate that proton transfer in these experiments is slow relative to the time scale of electrochemistry. With some bases, redox events for the PCET and fully protonated/deprotonated cluster could be observed simultaneously; we propose that this is due to a lower local concentration of base at the electrode surface, or slow proton transfer kinetics. For all measurements reported, it is assumed that half an equivalent of available base is consumed at the electrode at the PCET $E_{½}$ potential; making the observed potential based only on the redox potential of the Mn–OH_x cluster, and the pK_a of the added base.[9] All THF pK_a values used here were obtained from a report by Rosés and co-workers.[8]

Base with **2-[$BAr^F{}_4$]**	pK_a (THF)	$E_{½}(1)$ (V)	$E_{½}(2)$ (V)	$E_{½}(3)$ (V)
2-methyl-aniline	7.5	-0.885	-0.002 (-0.266)	
2-methyl-pyridine	8.6	-0.891	-0.028	0.327
2,6-dimethyl-pyridine	9.5	-0.894	-0.082	
2,4,6-trimethyl-pyridine	10.4	-0.907	-0.390	
triethylamine	14.9	-0.900	-0.373	
2-phenyl-1,1,3,3-tetramethylguanidine	16.5	-0.956	-0.468	
1,1,3,3-tetramethylguanidine	17.8	-1.034	-0.454	
1,8-diazabicyclo[5.4.0]undec-7-ene	19.1	-1.066	-0.468	
7-methyl-1,5,7-triazabicyclo[4.4.0]dec-5-ene	20.5	-1.148	-0.460	
1,5,7-triazabicyclo[4.4.0]dec-5-ene	22.0	-1.180	-0.451	
tert-butylimino-tri(pyrrolidino)phosphorane	22.8	-1.271	-0.461	
1-ethyl-2,2,4,4,4-pentakis(dimethylamino)2-λ^5,4λ^5-catenadi(phosphazene)	28.1	-1.317	-0.453	
Base with **6-[$BAr^F{}_4$]**				
tert-butylimino-tri(pyrrolidino)phosphorane	22.8	-1.307	-0.517	0.245
1-ethyl-2,2,4,4,4-pentakis(dimethylamino)2-λ^5,4λ^5-catenadi(phosphazene)	28.1	-1.333	-0.449	0.403

Table S3. Summary of observed $E_{½}$ potentials with organic bases of various pK_a values. All reported potentials referenced to Fc/Fc^+.

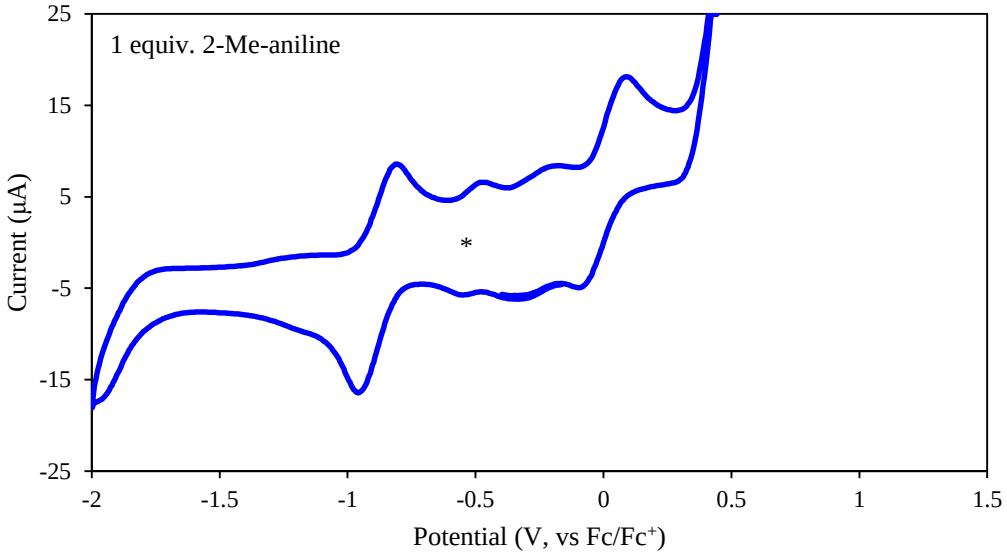

Figure S31. Cyclic voltammogram of $[LFe_3O(Pz)_3Mn][BAr^F{}_4]_2$ (**2-[BAr$^F{}_4$]**, 2 mM) in THF [250 mM H_2O] and 100 mM $[^nPr_4N][BAr^F{}_4]$ upon addition of 1 equivalent 2-methyl-aniline (pK_a(THF) = 7.5) at a scan rate of 50 mV/s. Asterisk (*) denotes redox couple of the decamethylferrocene internal standard. The open circuit potential was -0.4 V.

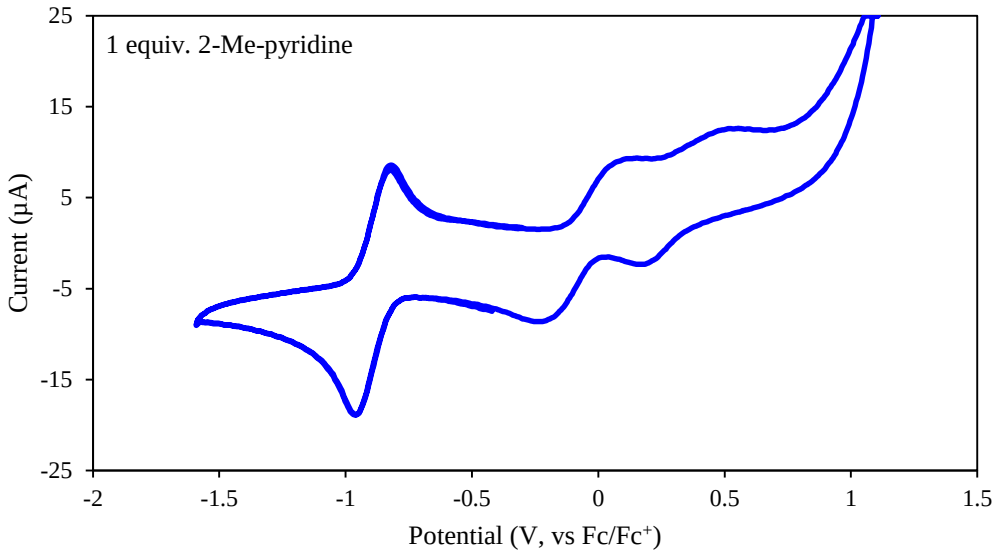

Figure S32. Cyclic voltammogram of $[LFe_3O(Pz)_3Mn][BAr^F{}_4]_2$ (**2-[BAr$^F{}_4$]**, 2 mM) in THF [250 mM H_2O] and 100 mM $[^nPr_4N][BAr^F{}_4]$ upon addition of 1 equivalent 2-methyl-pyridine (pK_a(THF) = 8.6) at a scan rate of 50 mV/s. An independent scan in the presence of a decamethylferrocene internal standard was used as a reference. The open circuit potential was -0.3 V.

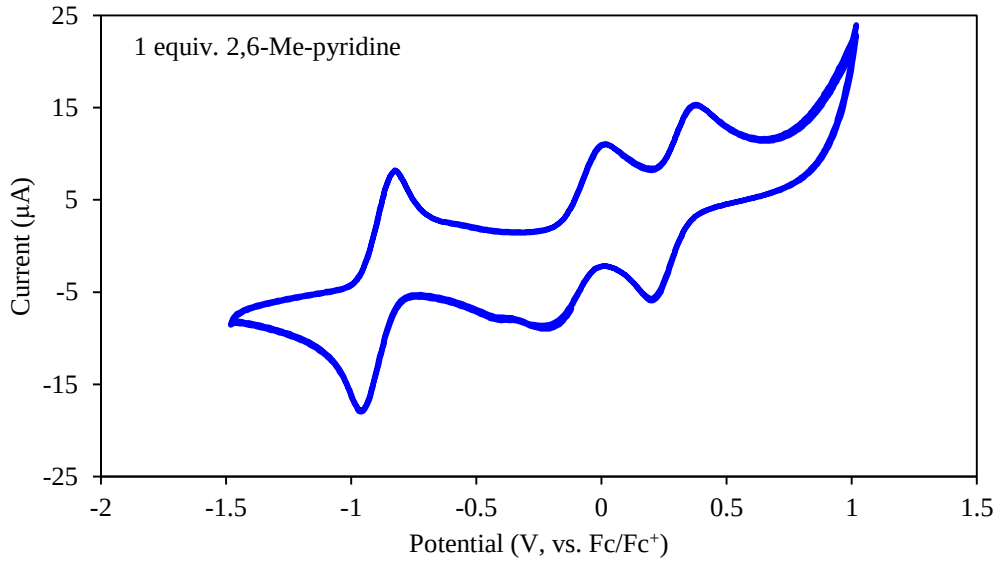

Figure S33. Cyclic voltammogram of $[LFe_3O(Pz)_3Mn][BAr^F{}_4]_2$ (**2-[BAr$^F{}_4$]**, 2 mM) in THF [250 mM H_2O] and 100 mM $[^nPr_4N][BAr^F{}_4]$ upon addition of 1 equivalent 2,6-dimethyl-pyridine (pK_a(THF) = 9.5) at a scan rate of 50 mV/s. An independent scan in the presence of a decamethylferrocene internal standard was used as a reference. The open circuit potential was -0.3 V.

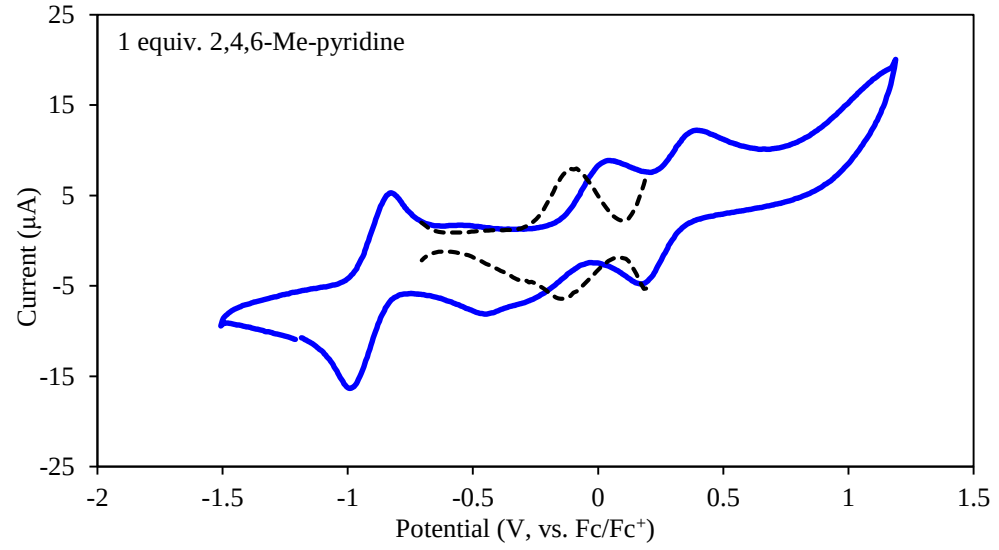

Figure S34. Cyclic voltammogram of $[LFe_3O(Pz)_3Mn][BAr^F{}_4]_2$ (**2-[BAr$^F{}_4$]**, 2 mM) in THF [250 mM H_2O] and 100 mM $[^nPr_4N][BAr^F{}_4]$ upon addition of 1 equivalent 2,4,6-trimethyl-pyridine (pK_a(THF) = 10.4) at a scan rate of 50 mV/s. An independent scan in the presence of a decamethylferrocene internal standard was used as a reference. The open circuit potential was -0.3 V. The $E_{½}$ of middle peak was determined via square wave voltammetry since its return wave was low in current, and overlapping with another peak.

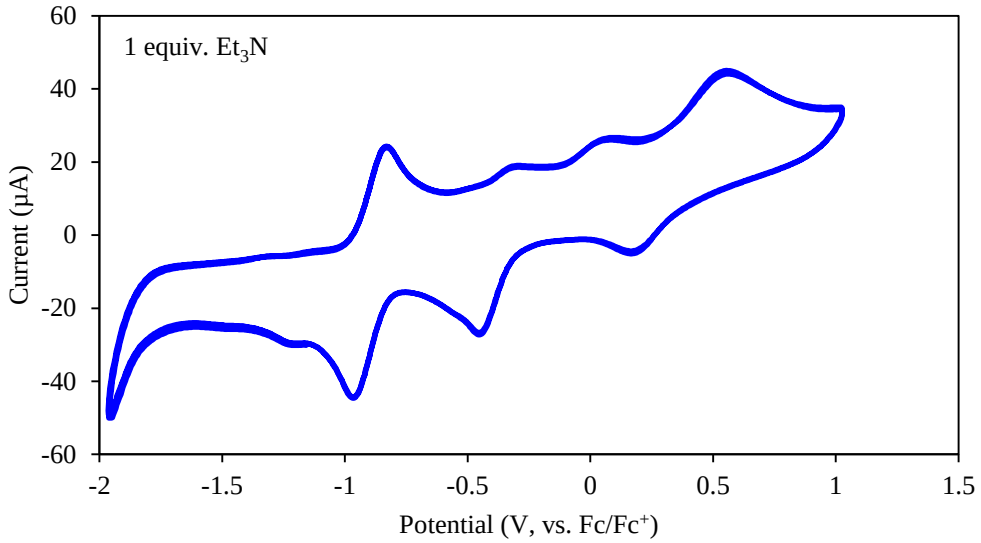

Figure S35. Cyclic voltammogram of $[LFe_3O(Pz)_3Mn][BAr^F{}_4]_2$ (**2-[BAr$^F{}_4$]**, 2 mM) in THF [250 mM H_2O] and 100 mM $[^nPr_4N][BAr^F{}_4]$ upon addition of 1 equivalent triethylamine (pK_a(THF) = 14.9) at a scan rate of 200 mV/s. An independent scan in the presence of a ferrocene internal standard was used as a reference. The open circuit potential was -0.6 V.

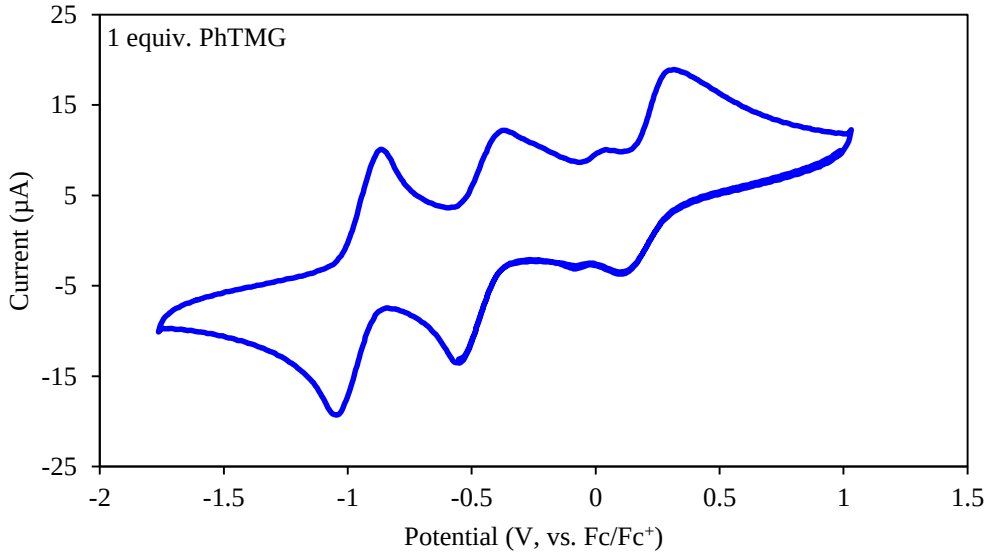

Figure S36. Cyclic voltammogram of $[LFe_3O(Pz)_3Mn][BAr^F{}_4]_2$ (**2-[BAr$^F{}_4$]**, 2 mM) in THF [250 mM H_2O] and 100 mM $[^nPr_4N][BAr^F{}_4]$ upon addition of 1 equivalent 2-phenyl-1,1,3,3-tetramethylguanidine (pK_a(THF) = 16.5) at a scan rate of 50 mV/s. An independent scan in the presence of a ferrocene internal standard was used as a reference. The open circuit potential was -0.7 V.

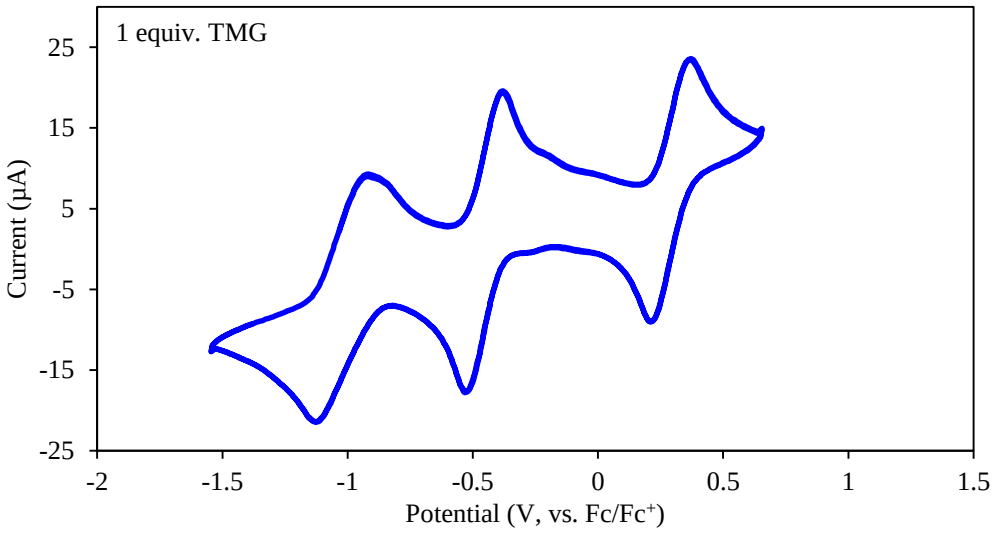

Figure S37. Cyclic voltammogram of $[LFe_3O(Pz)_3Mn][BAr^F{}_4]_2$ (**2-[BAr$^F{}_4$]**, 2 mM) in THF [250 mM H_2O] and 100 mM $[^nPr_4N][BAr^F{}_4]$ upon addition of 1 equivalent 1,1,3,3-tetramethylguanidine (pK_a(THF) = 17.8) at a scan rate of 50 mV/s. An independent scan in the presence of a ferrocene internal standard was used as a reference. The open circuit potential was -0.5 V.

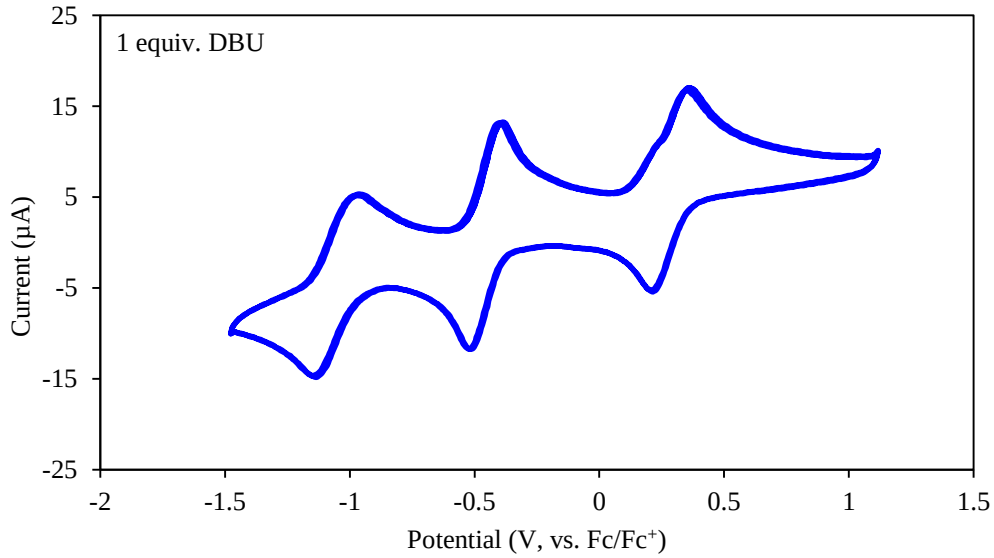

Figure S38. Cyclic voltammogram of $[LFe_3O(Pz)_3Mn][BAr^F{}_4]_2$ (**2-[BAr$^F{}_4$]**, 2 mM) in THF [250 mM H_2O] and 100 mM $[^nPr_4N][BAr^F{}_4]$ upon addition of 1 equivalent 1,8-diazabicyclo[5.4.0]undec-7-ene (pK_a(THF) = 19.1) at a scan rate of 50 mV/s. An independent scan in the presence of a ferrocene internal standard was used as a reference. The open circuit potential was -0.7 V.

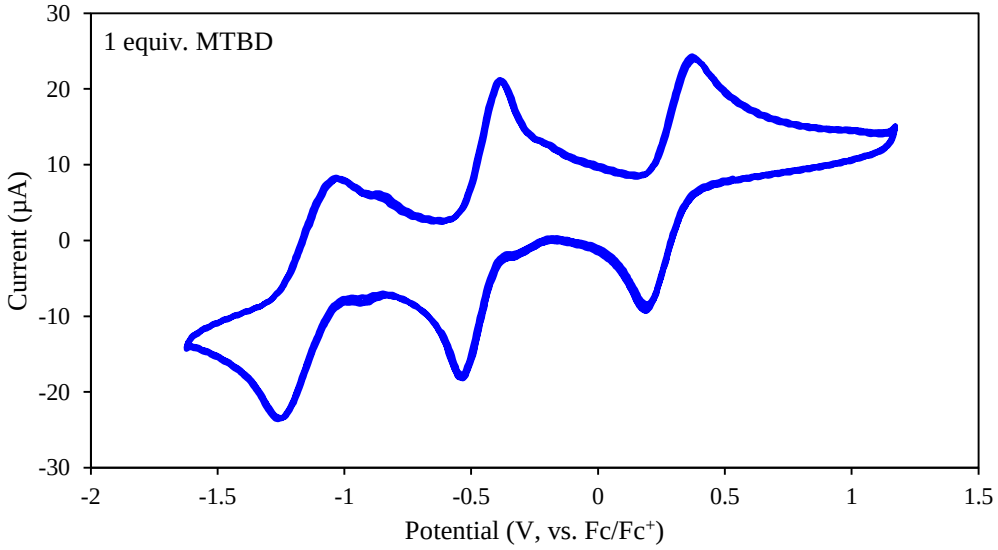

Figure S39. Cyclic voltammogram of $[LFe_3O(Pz)_3Mn][BAr^F{}_4]_2$ (**2-[BAr$^F{}_4$]**, 2 mM) in THF [250 mM H_2O] and 100 mM $[^nPr_4N][BAr^F{}_4]$ upon addition of 1 equivalent 7-methyl-1,5,7-triazabicyclo[4.4.0]dec-5-ene (pK_a(THF) = 20.5) at a scan rate of 50 mV/s. An independent scan in the presence of a ferrocene internal standard was used as a reference. The open circuit potential was -0.7 V.

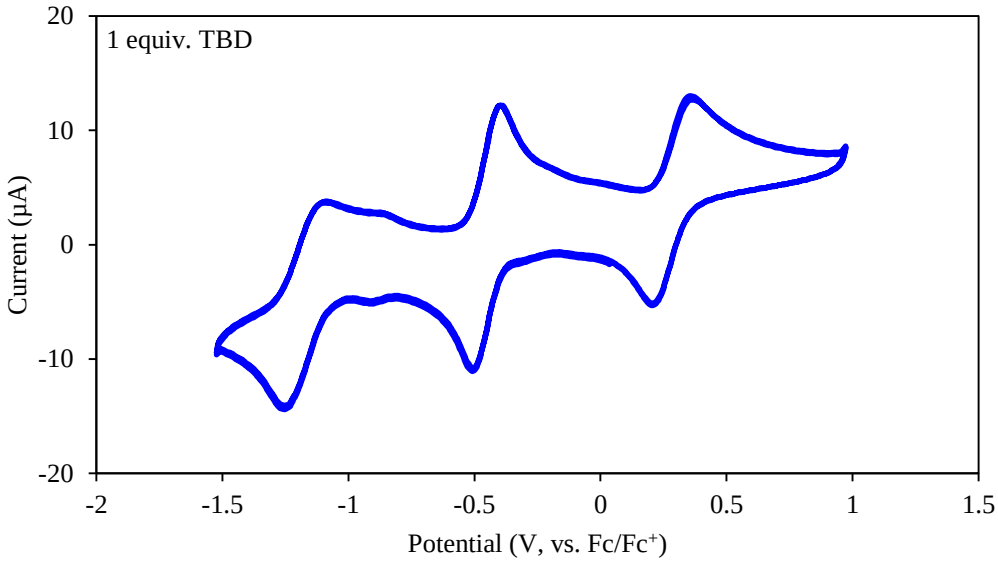

Figure S40. Cyclic voltammogram of $[LFe_3O(Pz)_3Mn][BAr^F{}_4]_2$ (**2-[BAr$^F{}_4$]**, 2 mM) in THF [250 mM H_2O] and 100 mM $[^nPr_4N][BAr^F{}_4]$ upon addition of 1 equivalent 1,5,7-triazabicyclo[4.4.0]dec-5-ene (pK_a(THF) = 22.0) at a scan rate of 50 mV/s. An independent scan in the presence of a ferrocene internal standard was used as a reference. The open circuit potential was -0.7 V.

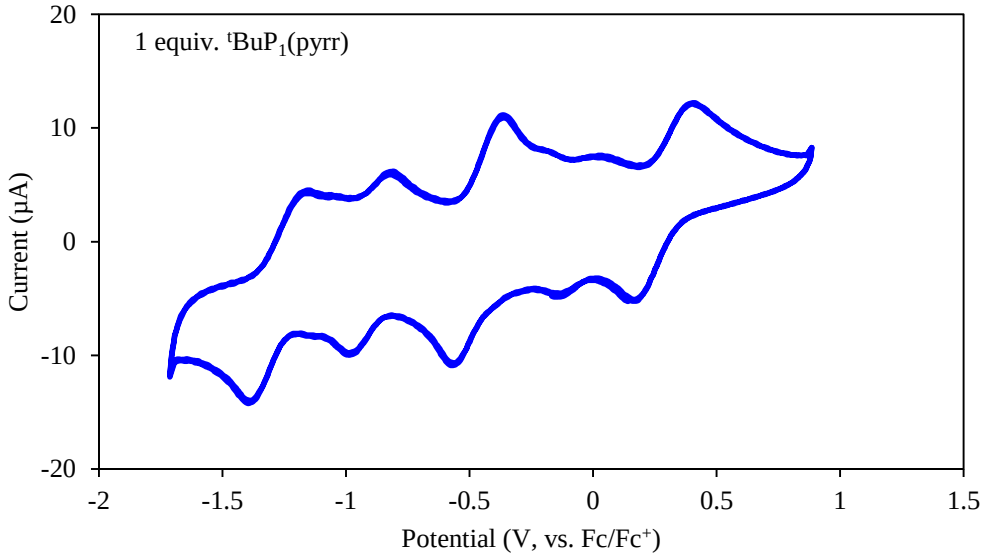

Figure S41. Cyclic voltammogram of $[LFe_3O(Pz)_3Mn][BAr^F{}_4]_2$ (**2-[BAr$^F{}_4$]**, 2 mM) in THF [250 mM H_2O] and 100 mM $[^nPr_4N][BAr^F{}_4]$ upon addition of 1 equivalent *tert*-butylimino-tri(pyrrolidino)phosphorane (pK_a(THF) = 22.8) at a scan rate of 50 mV/s. An independent scan in the presence of a ferrocene internal standard was used as a reference. The open circuit potential was -0.7 V.

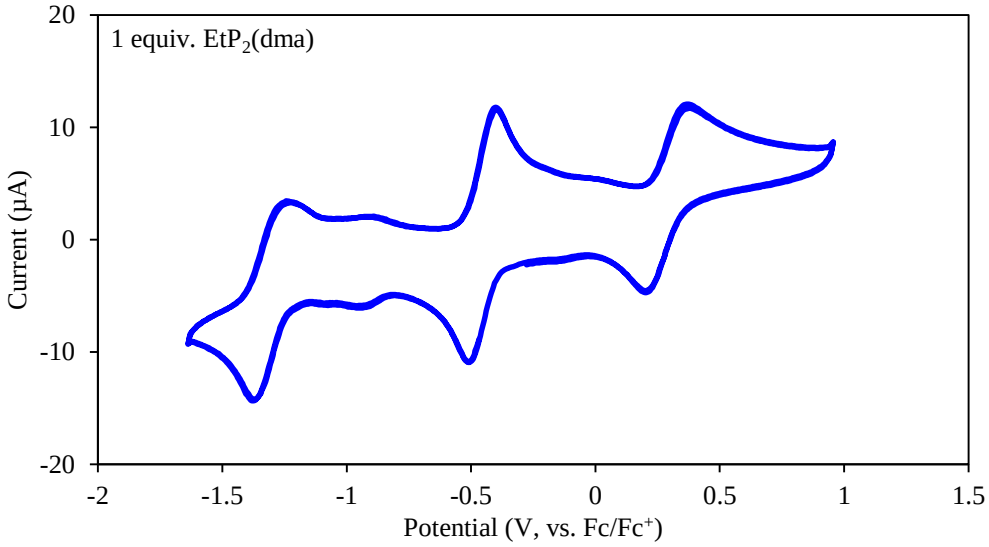

Figure S42. Cyclic voltammogram of $[LFe_3O(Pz)_3Mn][BAr^F{}_4]_2$ (**2-[BAr$^F{}_4$]**, 2 mM) in THF [250 mM H_2O] and 100 mM $[^nPr_4N][BAr^F{}_4]$ upon addition of 1 equivalent 1-ethyl-2,2,4,4,4-pentakis(dimethylamino)2λ^5,4λ^5-catenadi(phosphazene) (pK_a(THF) = 28.1) at a scan rate of 50 mV/s. An independent scan in the presence of a ferrocene internal standard was used as a reference. The open circuit potential was -0.7 V.

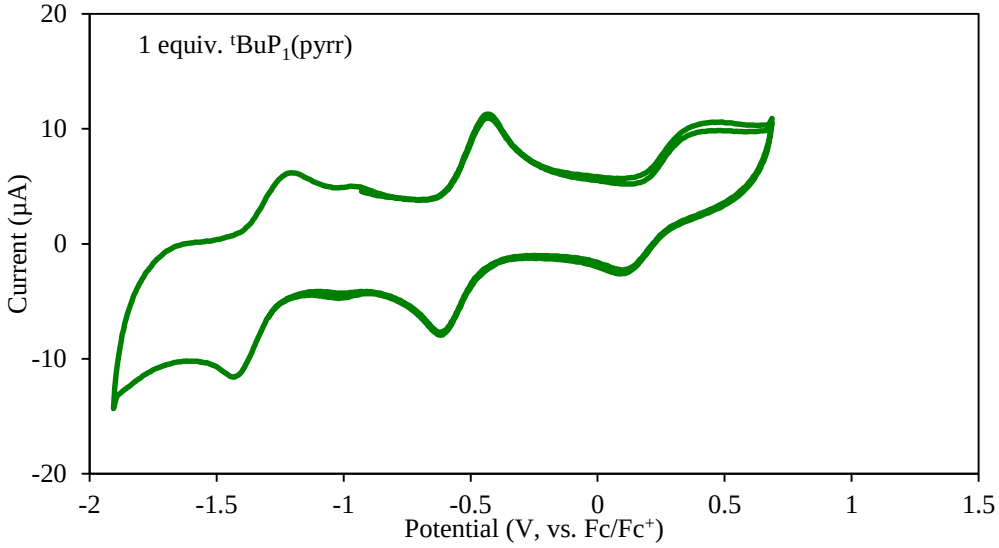

Figure S43. Cyclic voltammogram of $[LFe_3O(Pz)_3Mn(OH)][BAr^F_4]$ (**6-[BAr$^F_4$]**, 2 mM) in THF [250 mM H_2O] and 100 mM $[^nPr_4N][BAr^F_4]$ upon addition of 1 equivalent *tert*-butylimino-tri(pyrrolidino)phosphorane (pK_a(THF) = 22.8) at a scan rate of 50 mV/s. An independent scan in the presence of a ferrocene internal standard was used as a reference. The open circuit potential was -1.3 V.

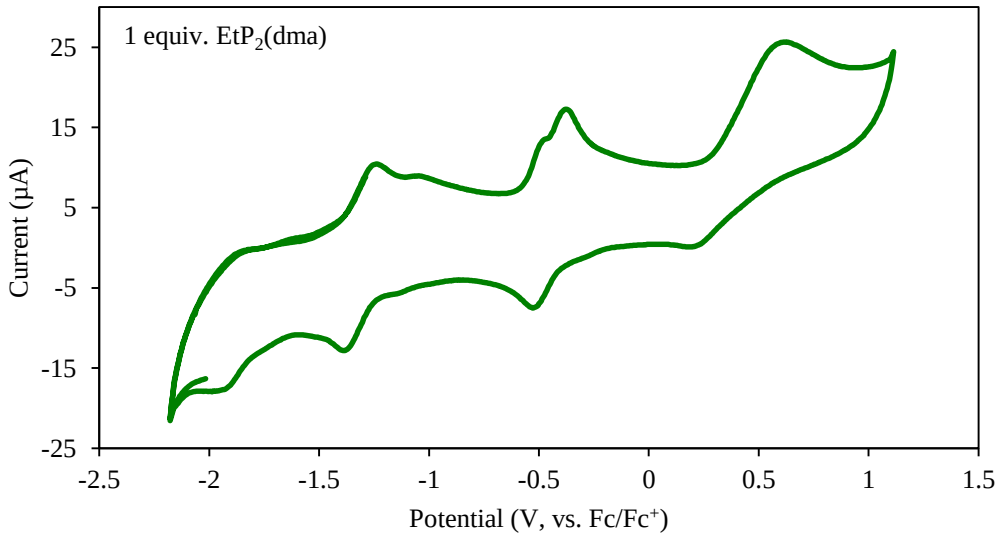

Figure S44. Cyclic voltammogram of $[LFe_3O(Pz)_3Mn(OH)][BAr^F_4]$ (**6-[BAr$^F_4$]**, 2 mM) in THF [250 mM H_2O] and 100 mM $[^nPr_4N][BAr^F_4]$ upon addition of 1 equivalent 1-ethyl-2,2,4,4,4-pentakis(dimethylamino)2λ^5,4λ^5-catenadi(phosphazene) (pK_a(THF) = 28.1) at a scan rate of 50 mV/s. An independent scan in the presence of a ferrocene internal standard was used as a reference. The open circuit potential was -1.3 V.

Mössbauer simulation details for all compounds. All spectra were simulated by three pairs of symmetric quadrupole doublets with equal populations and Lorentzian lineshapes. They were refined to a minimum via least squares optimization (13 fitting parameters per spectrum). Signals appearing above 2 mm/s were indicative with the presence of high-spin Fe^{II} centers and correspond to species with isomer shifts of ~ 1 mm/s. The Mössbauer data were fit to be consistent with our previously reported iron clusters.[1, 10-12] The observed Mossbauer parameters are in agreement with related six-coordinate high-spin Fe^{II}/Fe^{III} centers.[13-16]

Simulation details for 1-[OTf]: The spectrum displays three discernable peaks corresponding to two quadrupole doublets in ~ 1:2 ratio (Figure S45). The parameters of the more intense peak are consistent with a high-spin Fe(II) assignment, while the smaller doublet displays parameters consistent with high-spin Fe(III). The final fit split the large doublet into two equal signals (Figure S46).

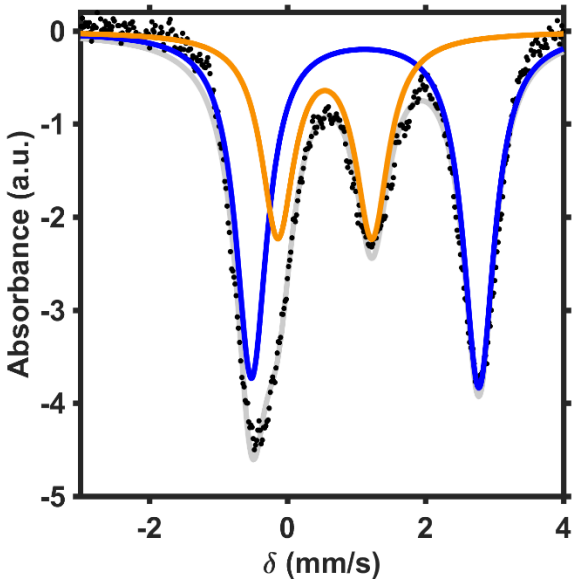

Figure S45. Mössbauer spectrum of **1-[OTf]** (black dots) fit with two doublets in a ~1:2 ratio (gray trace) with parameters δ = 0.543 mm/s; ΔE_q = 1.366 mm/s (orange trace) and δ = 1.126 mm/s; ΔE_q = 3.294 mm/s (blue trace).

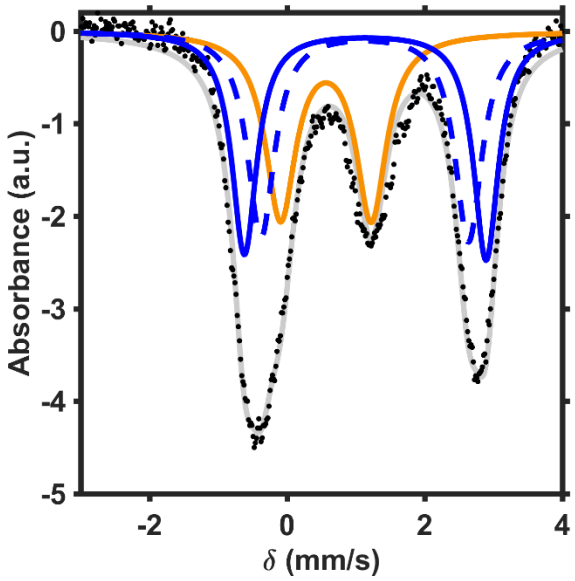

	δ (mm/s)	$\|\Delta E_q\|$ (mm/s)	Rel. %
———	1.135	3.513	33
– – –	1.127	3.016	33
———	0.563	1.318	33

Figure S46. Zero applied field Mössbauer spectrum of **1-[OTf]** (black dots) fit with three quadrupole doublets. The blue traces are assigned to high-spin Fe(II) and the orange trace is assigned as high-spin Fe(III).

Simulation details for 2-[OTf]: The spectrum displays four discernable peaks corresponding to two quadrupole doublets in ~ 1:2 ratio (Figure S47). The parameters of the more intense peak are consistent with a high-spin Fe(III) assignment, while the smaller doublet displays parameters consistent with high-spin Fe(II). The final fit split the large doublet into two equal signals (Figure S48).

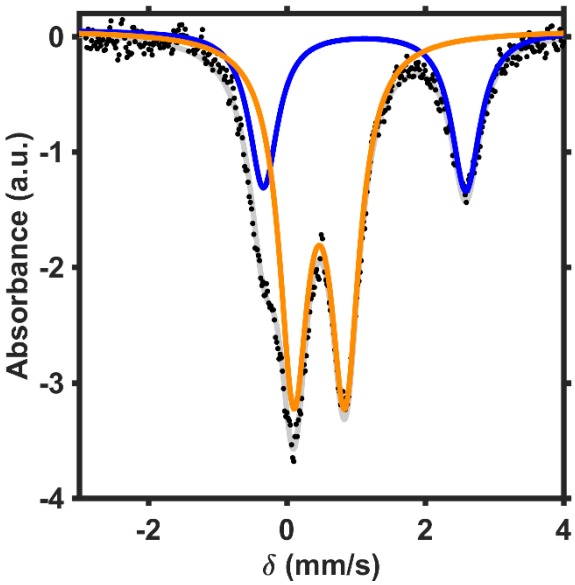

Figure S47. Mössbauer spectrum of **2-[OTf]** (black dots) fit with two doublets in a ~1:2 ratio (gray trace) with parameters δ = 0.469 mm/s; ΔE_q = 0.740 mm/s (orange trace) and δ = 1.124 mm/s; ΔE_q = 2.926 mm/s (blue trace).

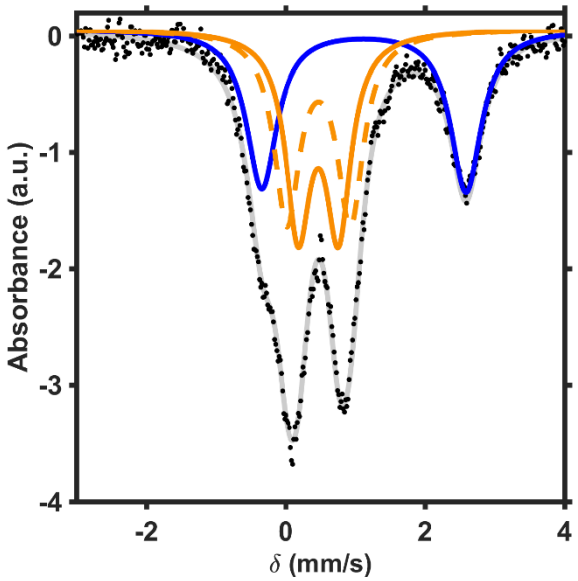

	δ (mm/s)	$\lvert\Delta E_q\rvert$ (mm/s)	Rel. %
	1.119	2.931	33
	0.468	0.578	33
	0.423	0.913	33

Figure S48. Zero applied field Mössbauer spectrum of **2-[OTf]** (black dots) fit with three quadrupole doublets. The blue trace is assigned to high-spin Fe(II) and the orange traces are assigned to high-spin Fe(III).

Simulation details for 3-[OTf]: The spectrum displays a single quadrupole doublet signal. Although three Fe(III) signals are expected, the best fit was obtained with only one set of parameters (Figure S49).

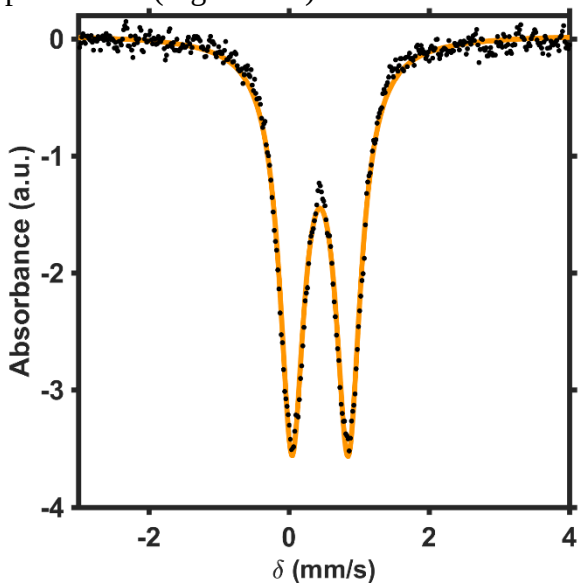

	δ (mm/s)	$\lvert\Delta E_q\rvert$ (mm/s)	Rel. %
	0.443	0.804	100

Figure S49. Zero applied field Mössbauer spectrum of **3-[OTf]** (black dots) fit to a single quadrupole doublet (orange trace); this signal is assigned to the high-spin Fe(III) centers in the cluster.

Simulation details for 1-[BAr$^{F}_{4}$]: The spectrum displays three discernable peaks corresponding to two quadrupole doublets in ~ 1:2 ratio (Figure S50). The parameters of the more intense peak are consistent with a high-spin Fe(II) assignment, while the smaller doublet displays parameters consistent with high-spin Fe(III). The final fit split the large doublet into two equal signals (Figure S51).

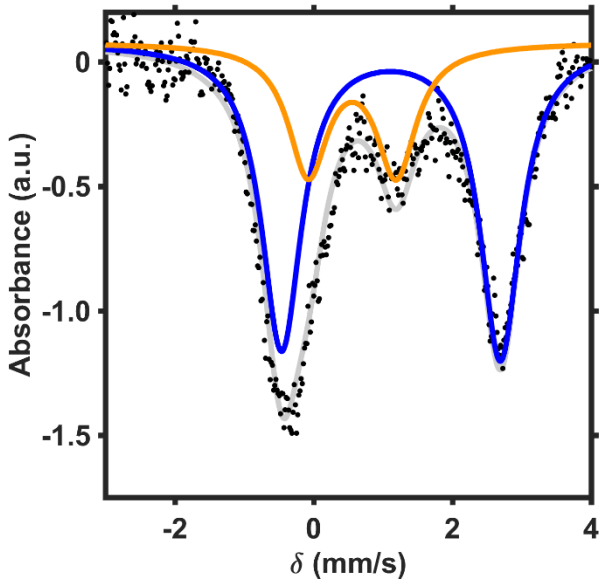

Figure S50. Mössbauer spectrum of **1-[BAr$^{F}_{4}$]** (black dots) fit with two doublets in a ~1:2 ratio (gray trace) with parameters δ = 0.556 mm/s; ΔE_q = 1.267 mm/s (orange trace) and δ = 1.115 mm/s; ΔE_q = 3.153 mm/s (blue trace).

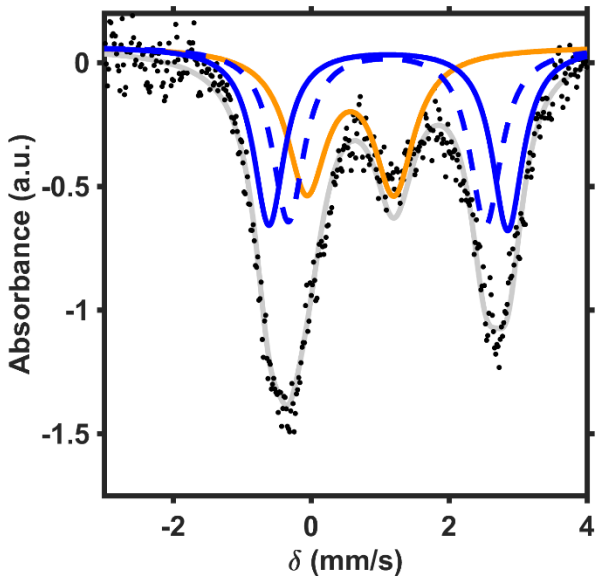

	δ (mm/s)	$\lvert\Delta E_q\rvert$ (mm/s)	Rel. %
———	1.119	3.460	33
– – –	1.099	2.860	33
———	0.570	1.266	33

Figure S51. Zero applied field Mössbauer spectrum of **1-[BAr$^{F}_{4}$]** (THF solution [250 mM H_2O]; black dots) fit with three quadrupole doublets. The blue traces are assigned to high-spin Fe(II) and the orange trace is assigned to high-spin Fe(III).

Simulation details for 2-[BAr$^{F}_{4}$]: The spectrum displays four discernable peaks corresponding to two quadrupole doublets in ~ 1:2 ratio (Figure S52). The parameters of the more intense peak are consistent with a high-spin Fe(III) assignment, while the smaller doublet displays parameters consistent with high-spin Fe(II). The final fit split the large doublet into two equal signals (Figure S53).

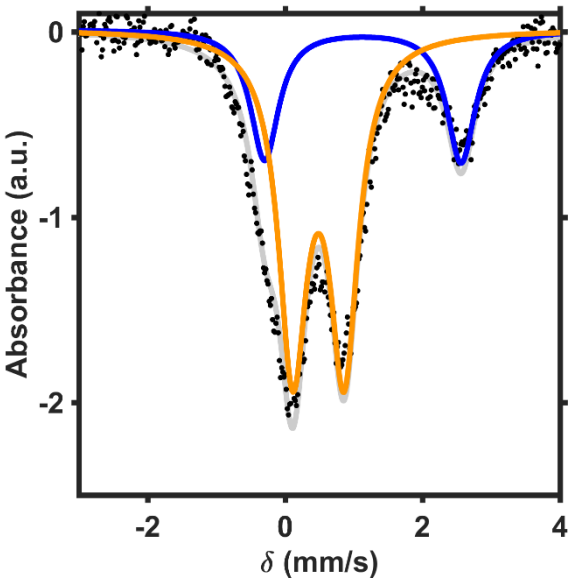

Figure S52. Mössbauer spectrum of **2-[BAr$^{F}_{4}$]** (black dots) fit with two doublets in a ~1:2 ratio (gray trace) with parameters δ = 0.485 mm/s; ΔE_q = 0.746 mm/s (orange trace) and δ = 1.132 mm/s; ΔE_q = 2.858 mm/s (blue trace).

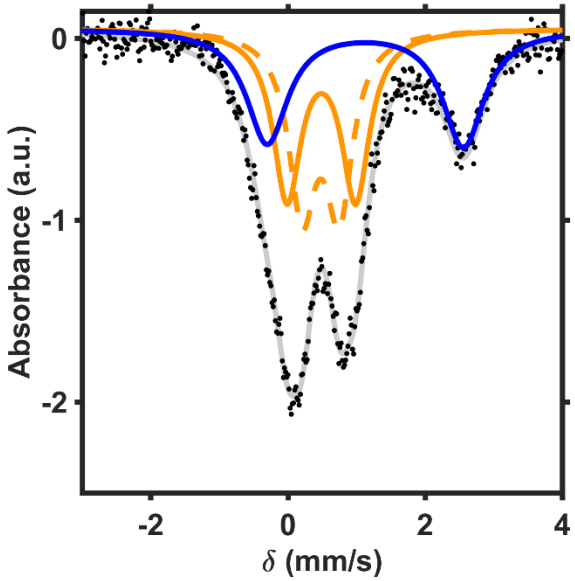

	δ (mm/s)	$\lvert\Delta E_q\rvert$ (mm/s)	Rel. %
———	1.128	2.858	33
———	0.487	0.999	33
– – –	0.478	0.540	33

Figure S53. Zero applied field Mössbauer spectrum of **2-[BAr$^{F}_{4}$]** (THF solution [250 mM H_2O]; black dots) fit with three quadrupole doublets. The blue trace is assigned to high-spin Fe(II) and the orange traces are assigned to high-spin Fe(III).

Simulation details for 3-[BAr$^{F}_{4}$]: The spectrum displays a single quadrupole doublet signal. Although three Fe(III) signals are expected, the best fit was obtained with only one set of parameters (Figure S54).

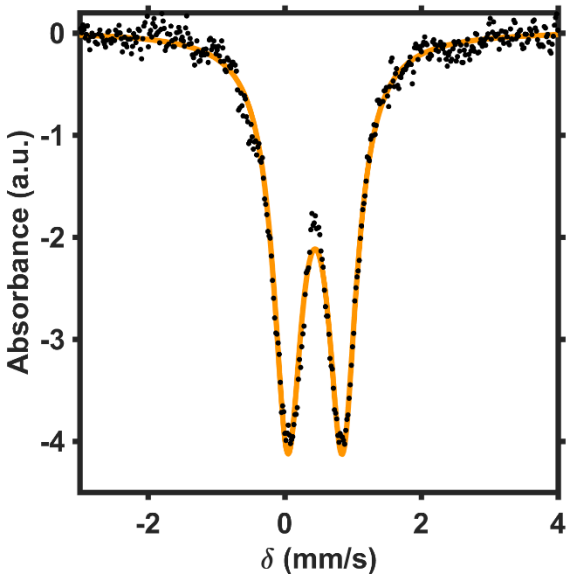

	δ (mm/s)	$\|\Delta E_q\|$ (mm/s)	Rel. %
	0.444	0.800	100

Figure S54. Zero applied field Mössbauer spectrum of **3-[BAr$^{F}_{4}$]** (THF solution [250 mM H_2O]; black dots) fit with a single quadrupole doublet assigned to high-spin Fe(III) centers.

Simulation details for 5: The spectrum displays an apparently asymmetric quadrupole doublet signal. The data could be fit to a single quadrupole doublet (Figure S55). The final fit split this signal into three equally abundant Fe(II) centers, to account for the asymmetry of the doublet (Figure S56).

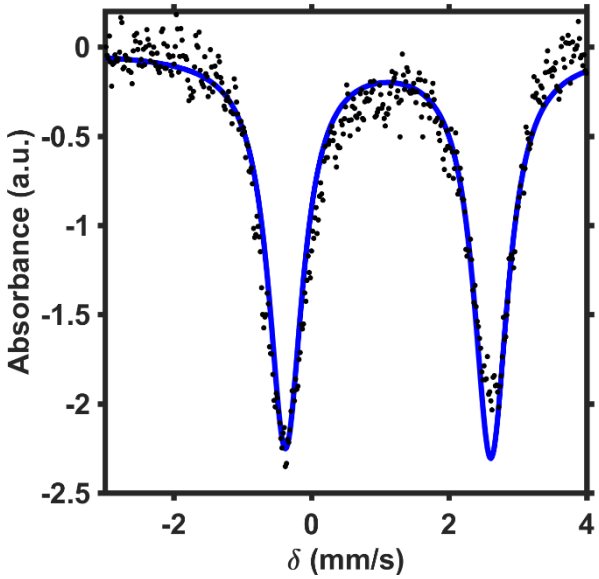

Figure S55. Mössbauer spectrum of **5** (black dots) fit with a single quadrupole doublet with parameters δ = 1.113 mm/s; ΔE_q = 2.985 mm/s (blue trace).

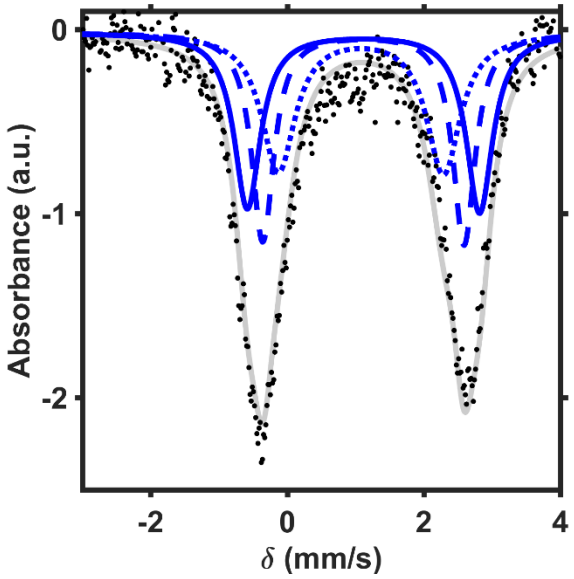

	δ (mm/s)	$\lvert\Delta E_q\rvert$ (mm/s)	Rel. %
———	1.115	3.399	33
– – –	1.115	2.947	33
·····	1.078	2.417	33

Figure S56. Zero applied field Mössbauer spectrum of **5** (black dots) fit with three quadrupole doublets. The blue traces are assigned to high-spin Fe(II).

Simulation details for 6-[BAr$^{F}_{4}$]: The spectrum displays four discernable peaks corresponding to two quadrupole doublets in ~ 1:2 ratio (Figure S57). The parameters of the more intense peak are consistent with a high-spin Fe(II) assignment, while the smaller doublet displays parameters consistent with high-spin Fe(III). The final fit split the large doublet into two equal signals (Figure S58).

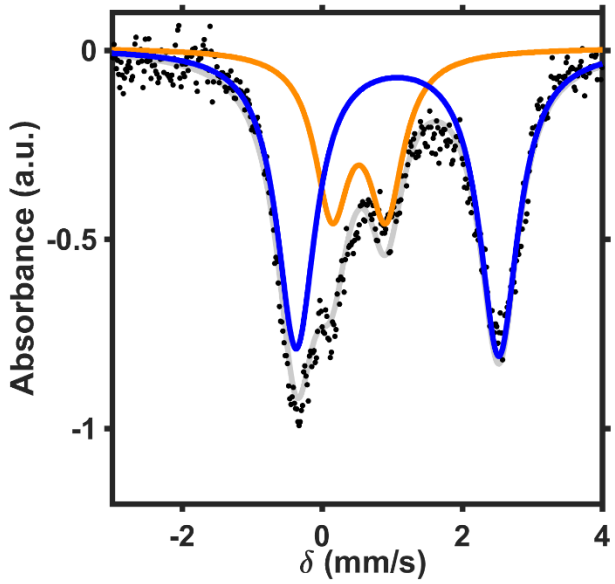

Figure S57. Mössbauer spectrum of **6-[BAr$^{F}_{4}$]** (black dots) fit with two doublets in a ~1:2 ratio (gray trace) with parameters δ = 0.525 mm/s; ΔE_q = 0.769 mm/s (orange trace) and δ = 1.075 mm/s; ΔE_q = 2.893 mm/s (blue trace).

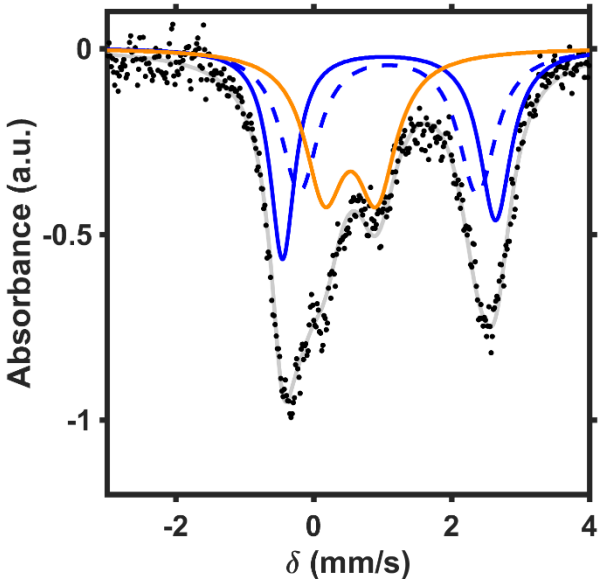

	δ (mm/s)	$\lvert\Delta E_q\rvert$ (mm/s)	Rel. %
———	1.093	3.091	33
– – –	1.083	2.576	33
———	0.534	0.756	33

Figure S58. Zero applied field Mössbauer spectrum of **6-[BAr$^{F}_{4}$]** (THF solution [250 mM H_2O]; black dots) fit with three quadrupole doublets. The blue traces are assigned to high-spin Fe(II) and the orange trace is assigned to high-spin Fe(III).

Simulation details for 7-[BAr$^{F}_{4}$]: The spectrum displays three discernable peaks, with a shoulder on the lowest peak, corresponding to two quadrupole doublets in ~ 1:2 ratio (Figure S59). The parameters of the more intense peak are consistent with a high-spin Fe(III) assignment, while the smaller doublet displays parameters consistent with high-spin Fe(III). The final fit split the large doublet into two equal signals (Figure S60).

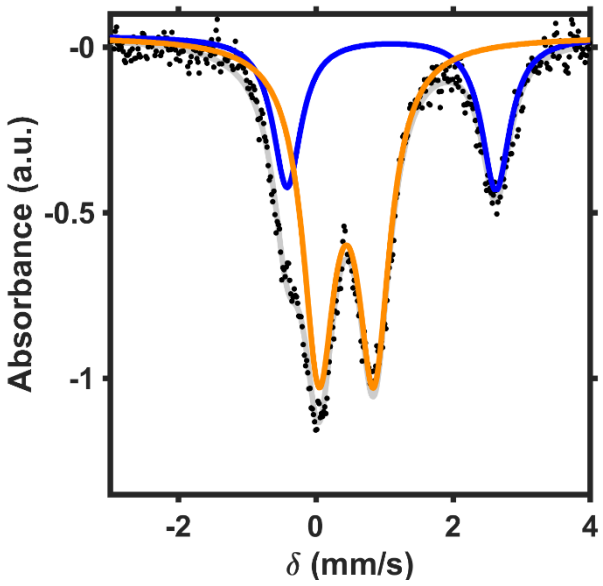

Figure S59. Mössbauer spectrum of **7-[BAr$^{F}_{4}$]** (black dots) fit with two doublets in a ~1:2 ratio (gray trace) with parameters δ = 0.447 mm/s; ΔE_q = 0.790 mm/s (orange trace) and δ = 1.109 mm/s; ΔE_q = 3.018 mm/s (blue trace).

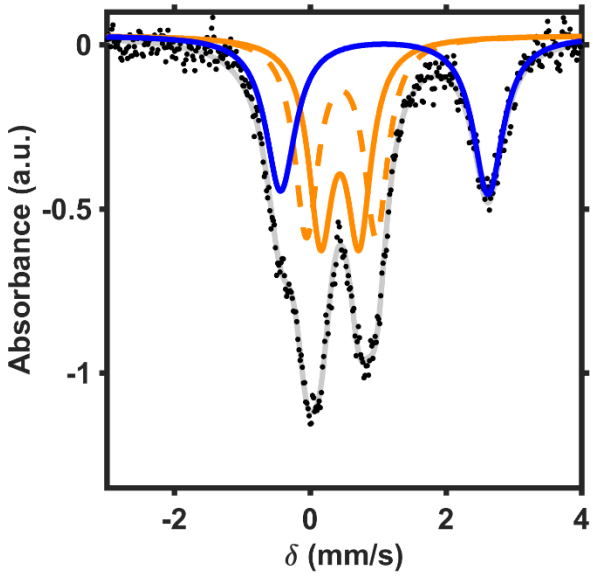

	δ (mm/s)	$\lvert\Delta E_q\rvert$ (mm/s)	Rel. %
———	1.096	3.033	33
———	0.434	0.547	33
– – –	0.462	1.019	33

Figure S60. Zero applied field Mössbauer spectrum of **7-[BAr$^{F}_{4}$]** (THF solution [250 mM H_2O]; black dots) fit with three quadrupole doublets. The blue trace is assigned to high-spin Fe(II) and the orange traces are assigned to high-spin Fe(III).

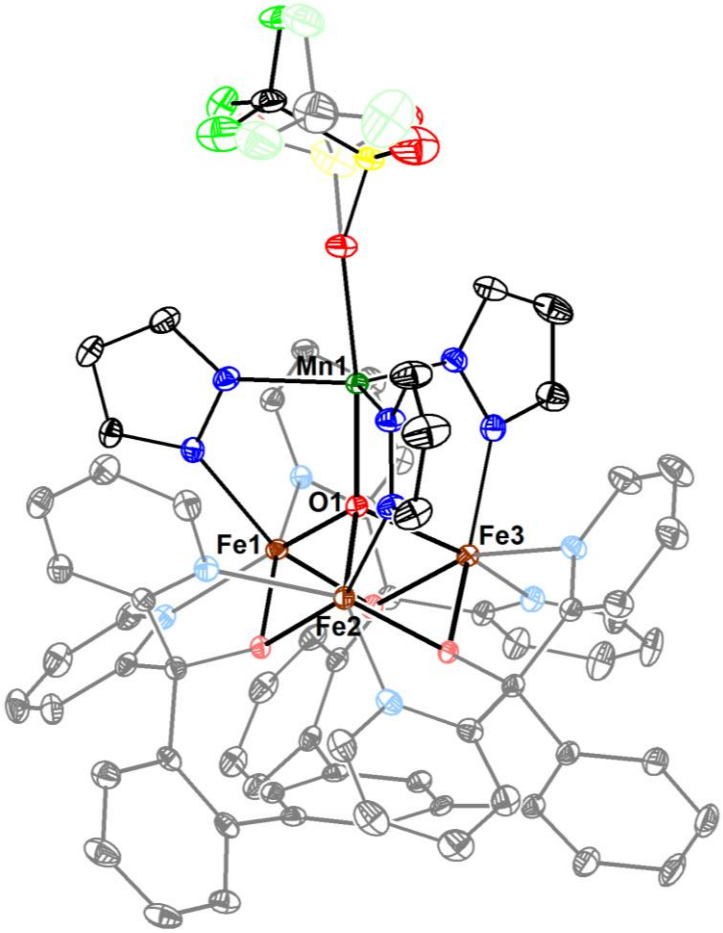

Figure S61. Crystal structure of [$LFe_3O(Pz)_3Mn$][OTf] (**1-[OTf]**). Ellipsoids are shown at the 50% probability level. Hydrogen atoms and solvent molecules are omitted for clarity.

Special refinement details for [$LFe_3O(Pz)_3Mn$][OTf]. The triflate counterion bound to Mn1 is disordered over two positions with refined occupancies of 12% (S200 through C200) and 88% (S201 through C201).

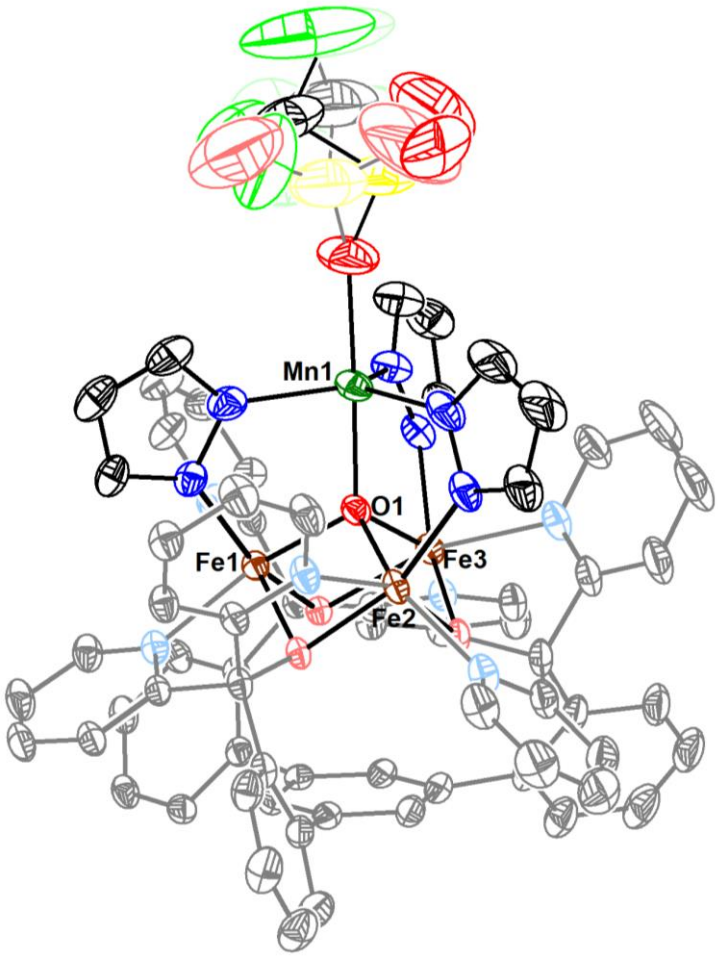

Figure S62. Crystal structure of $[LFe_3O(Pz)_3Mn][OTf]_2$ (**2-[OTf]**). Ellipsoids are shown at the 50% probability level. Hydrogen atoms, solvent molecules, and outersphere counterions are omitted for clarity.

Special refinement details for $[LFe_3O(Pz)_3Mn][OTf]_2$. The triflate counterion bound to Mn1 is disordered over two positions with refined occupancies of 51% (S200 through C200) and 49% (S201 through C201). A disordered THF molecule was modeled over two positions with occupancies of 81% (O102 through C107) and 19% (O101 through C111). A different THF molecule was modeled to be only partially occupied (56%; O103 through C115). A co-crystallized solvent site was modeled to contain a mixture of three different molecules: a THF (27% O105 through C123), a DCM (22%; Cl10 through C124), and Et_2O (64%; O104 through C119).

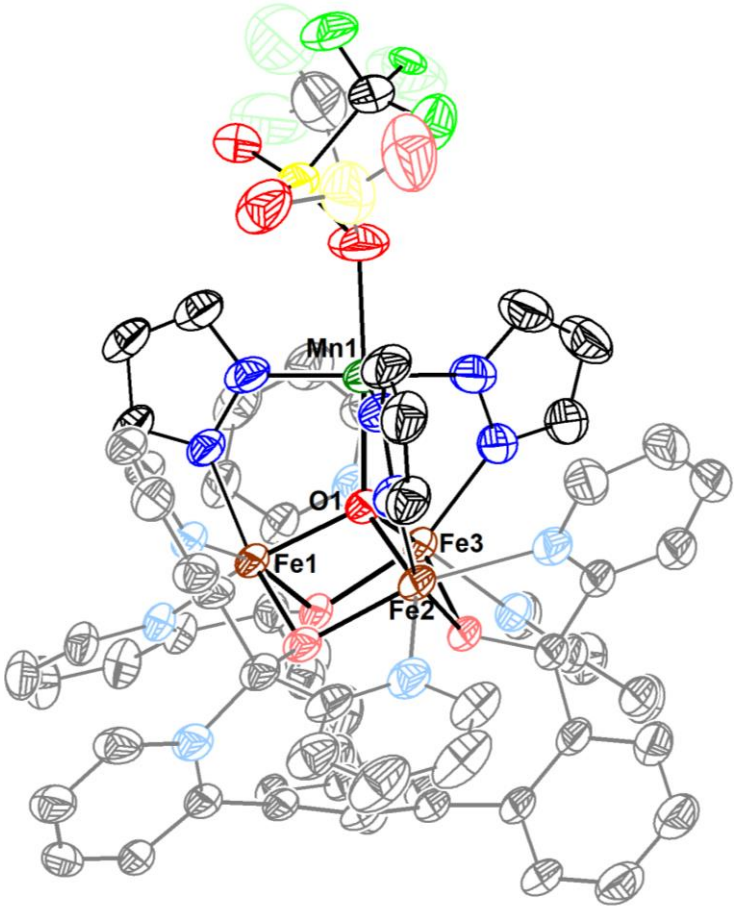

Figure S63. Crystal structure of $[LFe_3O(Pz)_3Mn][OTf]_3$ (**3-[OTf]**). Ellipsoids are shown at the 50% probability level. Hydrogen atoms, solvent molecules, and outersphere counterions are omitted for clarity.

Special refinement details for $[LFe_3O(Pz)_3Mn][OTf]_3$. The triflate counterion bound to Mn1 is disordered over two positions with refined occupancies of 30% (S200 through C200) and 70% (S201 through C201). An outersphere triflate was modeled in two different positions with occupancies of 38% (S203 through C203) and 62% (S204 through C204). For the S203 through C203 triflate, a nearby Et_2O molecule was modeled as partially occupied at 62%. For the S204 through C204, a nearby MeCN molecule was modeled as partially occupied at 38%.

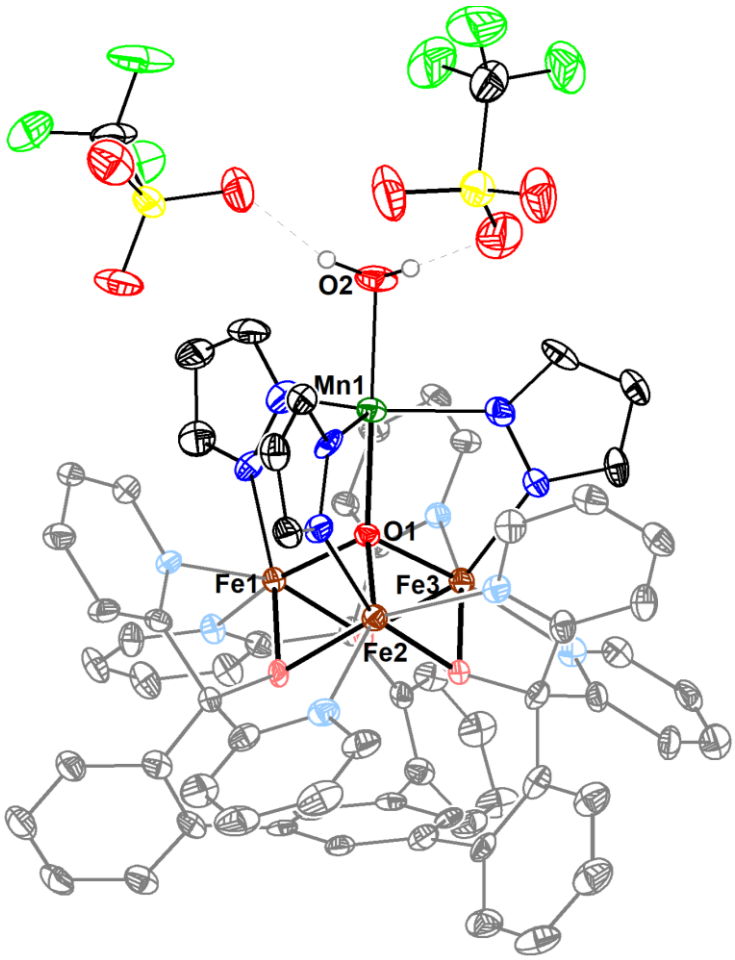

Figure S64. Crystal structure of $[LFe_3O(Pz)_3Mn(OH_2)][OTf]_2$ (**2-[OTf] (H_2O)**). Ellipsoids are shown at the 50% probability level. Hydrogen atoms and solvent molecules are omitted for clarity.

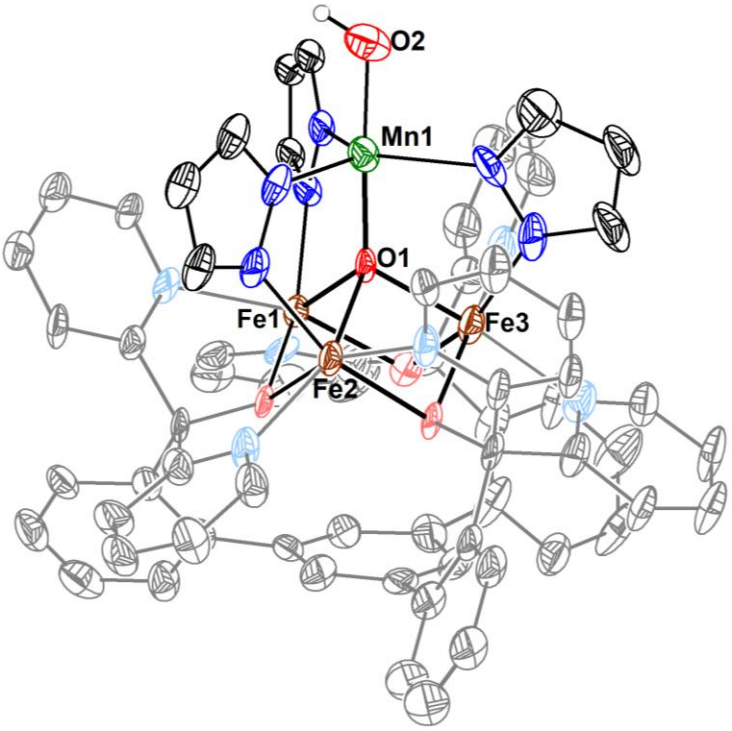

Figure S65. Crystal structure of [$LFe_3O(Pz)_3Mn(OH)$][OTf] (**6-[OTf]**). Ellipsoids are shown at the 50% probability level. Hydrogen atoms, solvent molecules, and outersphere counterions are omitted for clarity.

Special refinement details for [$LFe_3O(Pz)_3Mn(OH)$][OTf]. The outersphere triflate is disordered over two positions, modeled at an occupancy of 50% each. Both triflates are on symmetry elements and positionally disordered. For the S200 through C200 triflate, this was modeled with EXYZ/EADP constraints. For the S201 throughC201 triflate, the C and S atoms were constrained with EXYZ/EACDP, and the O203 through F205 atoms were modeled in alternating positions, at 50% occupancy each. A void in the structure was a mixture of different solvent molecules that couldn't be adequately modeled, and a solvent mask was used to account for this electron density.

	1-[OTf]	**2-[OTf]**	**3-[OTf]**
CCDC Number	1848679	1848681	1848680
Empirical	$C_{77}H_{62}F_3Fe_3MnN_{12}O_8S$	$C_{105.2}H_{81.2}BCl_{0.5}F_3Fe_3MnN_{12}O_{10.5}S$	$C_{76}H_{53.5}F_9Fe_3MnN_{13.4}O_{14.1}S_3$
Formula weight	1594.9	2019.8	1869.7
Radiation	MoKα (λ = 0.71073)	MoKα (λ = 0.71073)	CuKα (λ = 1.54178)
a (Å)	12.2741(5)	14.2908(12)	44.125(2)
b (Å)	19.4126(8)	15.9691(13)	14.3106(7)
c (Å)	15.5112(6)	24.3709(17)	24.8034(10)
α (°)	90	71.236(4)	90
β (°)	108.397(2)	75.366(2)	90.402(3)
γ (°)	90	70.262(4)	90
V (Å^3)	3507.0(2)	4891.6(7)	15661.9(13)
Z	2	2	8
Cryst. syst.	monoclinic	triclinic	monoclinic
Space group	$P2_1$	P-1	C2/c
ρ_{calc}g (cm^3)	1.510	1.371	1.586
2 σ range (°)	5.028 to 56.648	5.076 to 60.444	6.492 to 145.272
μ (mm^{-1})	0.899	0.668	7.226
GOF	1.031	1.029	1.037
R1, wR2 (I>2σ (I))	0.0244, 0.0583	0.0635, 0.1712	0.0840, 0.2131

	6-[OTf]	**2-[OTf] (H_2O)**
CCDC Number	1848678	1848677
Empirical formula	$C_{67}H_{49}F_3Fe_3MnN_{12}O_8S$	$C_{72}H_{62}F_6Fe_3MnN_{12}O_{13}S_2$
Formula weight	1461.7	1703.9
Radiation	CuKα (λ = 1.54178)	CuKα (λ = 1.54178)
a (Å)	14.7283(7)	12.2685(6)
b (Å)	19.3808(10)	29.896(2)
c (Å)	45.518(2)	19.6152(17)
α (°)	90	90
β (°)	92.474(3)	92.393(5)
γ (°)	90	90
V (Å^3)	12980.9(11)	7188.2(9)
Z	8	4
Cryst. syst.	monoclinic	monoclinic
Space group	C2/c	$P2_1/c$
ρ_{calc}g (cm^3)	1.496	1.575
2 σ range (°)	7.544 to 132.498	5.392 to 149.51
μ (mm^{-1})	7.742	7.461
GOF	1.160	1.140
R1, wR2 (I>2σ (I))	0.1305, 0.2771	0.1109, 0.2060

Table S4. Crystal and refinement data for complexes **1-[OTf]** – **3-[OTf], 2-[OTf] (H_2O)** and **6-[OTf]**.

References

1. de Ruiter G, Thompson NB, Lionetti D, Agapie T. Nitric Oxide Activation by Distal Redox Modulation in Tetranuclear Iron Nitrosyl Complexes. *Journal of the American Chemical Society.* **2015**; *137*, 14094.

2. Riedel PJ, Arulsamy N, Mehn MP. Facile routes to manganese(II) triflate complexes. *Inorganic Chemistry Communications.* **2011**; *14*, 734.

3. Izod K, Rayner DG, El-Hamruni SM, Harrington RW, Baisch U. Stabilization of a Diphosphagermylene through pπ–pπ Interactions with a Trigonal-Planar Phosphorus Center. *Angewandte Chemie International Edition.* **2014**; *53*, 3636.

4. Huang C-Y, Doyle AG. Nickel-Catalyzed Negishi Alkylations of Styrenyl Aziridines. *Journal of the American Chemical Society.* **2012**; *134*, 9541.

5. Zhang Y, Santos AM, Herdtweck E, Mink J, Kuhn FE. Organonitrile ligated silver complexes with perfluorinated weakly coordinating anions and their catalytic application for coupling reactions. *New Journal of Chemistry.* **2005**; *29*, 366.

6. Manner VW, Markle TF, Freudenthal JH, Roth JP, Mayer JM. The first crystal structure of a monomeric phenoxyl radical: 2,4,6-tri-tert-butylphenoxyl radical. *Chemical Communications.* **2008**, 256.

7. Thomson RK, Scott BL, Morris DE, Kiplinger JL. Synthesis, structure, spectroscopy and redox energetics of a series of uranium(IV) mixed-ligand metallocene complexes. *Comptes Rendus Chimie.* **2010**; *13*, 790.

8. Garrido G, Koort E, Ràfols C, Bosch E, Rodima T, Leito I, Rosés M. Acid−Base Equilibria in Nonpolar Media. Absolute pKa Scale of Bases in Tetrahydrofuran. *The Journal of Organic Chemistry.* **2006**; *71*, 9062.

9. McCarthy BD, Dempsey JL. Decoding Proton-Coupled Electron Transfer with Potential–pKa Diagrams. *Inorganic Chemistry.* **2017**; *56*, 1225.

10. de Ruiter G, Thompson NB, Takase MK, Agapie T. Intramolecular C–H and C–F Bond Oxygenation Mediated by a Putative Terminal Oxo Species in Tetranuclear Iron Complexes. *Journal of the American Chemical Society.* **2016**; *138*, 1486.

11. Herbert DE, Lionetti D, Rittle J, Agapie T. Heterometallic Triiron-Oxo/Hydroxo Clusters: Effect of Redox-Inactive Metals. *Journal of the American Chemical Society.* **2013**; *135*, 19075.

12. de Ruiter G, Carsch KM, Gul S, Chatterjee R, Thompson NB, Takase MK, Yano J, Agapie T. Accelerated Oxygen Atom Transfer and C−H Bond Oxygenation by Remote Redox Changes in Fe_3Mn-Iodosobenzene Adducts. *Angewandte Chemie International Edition.* **2017**; *56*, 4772.

13. Herold S, Lippard SJ. Synthesis, Characterization, and Magnetic Studies of Two Novel Isostructural Pentanuclear Iron(II) Complexes. *Inorganic Chemistry.* **1997**; *36,* 50.

14. Singh AK, Jacob W, Boudalis AK, Tuchagues J-P, Mukherjee R. A Tetragonal Core with Asymmetric Iron Environments Supported Solely by Bis(μ-OH){μ-(O–H···O)} Bridging and Terminal Pyridine Amide (N, O) Coordination: A New Member of the Tetrairon(III) Family. *European Journal of Inorganic Chemistry.* **2008**; *2008*, 2820.

15. Sutradhar M, Carrella LM, Rentschler E. A Discrete μ4-Oxido Tetranuclear Iron(III) Cluster. *European Journal of Inorganic Chemistry.* **2012**; *2012*, 4273.

16. Schünemann V, Hauke P. Mössbauer Spectroscopy. In: Scott RA, Lukehart CM, editors. Applications of Physical Methods to Inorganic and Bioinorganic Chemistry. West Sussex, England: John Wiley & Sons; 2007. p. 243.